C. R. Mecanique 347 (2019) 141–165

Contents lists available at ScienceDirect

Comptes Rendus Mecanique

www.sciencedirect.com

Performance of hydrodynamic journal bearing under the combined influence of textured surface and journal misalignment: A numerical survey

Belkacem Manser [a,*], Idir Belaidi [a], Abderrachid Hamrani [b], Sofiane Khelladi [c], Farid Bakir [c]

[a] LEMI, FSI, University of M'hamed Bougara, avenue de l'Indépendance, 35000 Boumerdes, Algeria
[b] Department of Bioresource Engineering, McGill University, Sainte-Anne-de-Bellevue, Montreal, QC, Canada
[c] DynFluid Lab., Arts et Métiers ParisTech, 151, boulevard de l'Hôpital, 75013 Paris, France

ARTICLE INFO

Article history:
Received 4 September 2018
Accepted after revision 6 November 2018
Available online 23 January 2019

Keywords:
Hydrodynamic journal bearing
JFO boundary conditions
Misalignment effect
Surface texturing
Dimple shapes

ABSTRACT

A wisely chosen geometry of micro textures with the favorable relative motion of lubricated surfaces in contacts can enhance tribological characteristics. In this paper, a computational investigation related to the combined influence of bearing surface texturing and journal misalignment on the performances of hydrodynamic journal bearings is reported. To this end, a numerical analysis is performed to test three texture shapes: square "SQ", cylindrical "CY", and triangular "TR", and shaft misalignment variation in angle and degree. The Reynolds equation of a thin viscous film is solved using a finite differences scheme and a mass conservation algorithm (JFO boundary conditions), taking into account the presence of textures on both full film and cavitation regions. Preliminary results are compared with benchmark data and are consistent with a positive enhancement in misaligned bearing performances (load carrying capacity and friction). The results suggest that the micro-step bearing mechanism is a key parameter, where the micro-pressure recovery action present in dimples located at the second angular part of the bearing (from 180° to 360°) can compensate for the loss on performances caused by shaft misalignment, while the micro-pressure drop effect at the full film region causes poor performances. Considering the right arrangement of textures on the contact surface, their contours geometries can have a significant impact on the performance of misaligned journal bearings, particularly at high eccentricity ratios, high misalignment degrees and when the misalignment angle α approaches to 0° or 180°.

© 2018 Académie des sciences. Published by Elsevier Masson SAS. All rights reserved.

1. Introduction

With the technological progress that has been achieved in recent years, rotating machinery such as electrical motors, generators, pumps, compressors, and high-speed machining spindles, etc., becomes increasingly powerful with higher rotation speed. Hydrodynamic rotor-bearing systems are important parts in present-day heavy machinery. Because of their

* Corresponding author.
E-mail address: b.manser@univ-boumerdes.dz (B. Manser).

https://doi.org/10.1016/j.crme.2018.11.002
1631-0721/© 2018 Académie des sciences. Published by Elsevier Masson SAS. All rights reserved.

efficiency, simplicity, high precision, low cost, long life, silent operation, low friction and wear and good heat dissipation [1], bearing systems are widely used in rotor systems and they usually correspond to the best existing technological designs in some rotating machines. One of the most commonly used industrial bearings are the radial-loaded hydrodynamic journal bearings, required to support heavy loads at high rotational speeds. However, they present the most important power losses in rotating machines [2]. It is well known that the misalignment is a disturbing factor that affects directly the operating conditions of journal bearings. Indeed, misalignment arise generally from: manufacturing tolerances, assembly errors, asymmetric bearing load, deflection of journal and bearing supports, improper installation and assembly errors, etc. In general, misalignment causes wear and vibration, reduces bearing performances and life, thus leading to system failure. Understanding the nature of misalignment has been the object of numerous theoretical and experimental studies [3]. The first one was recorded by McKee and McKee [4], where the influence of journal misalignment on the maximum pressure location was experimentally analyzed. DuBois et al. [5] reported that, under misalignment, the pressure distribution becomes asymmetric where the peak was located at the bearing ends. Subsequently, an experimental analysis about the effect of a known misalignment couple and eccentricity ratio on the proprieties of misaligned plain bearings was conducted [6]. Many theoretical studies were also carried out by many researchers in order to examine the effect of misalignment on the characteristics of various bearing systems. We can quote the following research examples for: plain bearings [7,8], partial bearings [9], gas bearings [10,11], tilting-pad journal bearing [12,13], hydrostatic journal bearing [14,15], two-lobe bearings [16] and three-lobe bearings [17], etc. In recent years, many works were devoted to the analysis of the combined effects of misalignment and influencing factors, such as bearing configuration, groove type and its location [18,19], cavitation effect [20,21], thermal effect [22,23], elastic and thermal deformation [24,25], porosity effect [26,27], turbulent effect [28,29], non-Newtonian lubricants [30,31], and water-lubricated plain journal bearings [32], etc.

In all the above theoretical studies, the analysis of misalignment was performed based on the assumptions of smooth surface bearings. Most recently, the tribology community has been interested in the effect of surface roughness on the performance of hydrodynamically lubricated contacts. Many works [33–36] were dedicated to the study of the combined influences of surface roughness and journal misalignment on bearing systems using either Christensen's stochastic theory of rough surfaces [20] or the average flow theory introduced by Patir and Cheng [37,38]. The conclusion was that the combined influence of bearing surface roughness and shaft misalignment is more pronounced at higher eccentricities [33], while other published encouraging results report that surface roughness may compensate for the decrease in minimum film thickness caused by shaft misalignment [35].

Nowadays, the emphasis has been placed on surface texturing and its effect on the performance characteristics of bearing systems. The idea is similar to the surface roughness, but in the case of surface texturing, the operator intentionally incorporates a well-defined dimple shape to obtain the desired tribological characteristics [39]. Moreover, with the development of manufacturing technology, particularly micro-fabrication techniques (laser surface texturing [40], reactive ion etching [41], LIGA process [42], vibro-rolling [43], vibro-mechanical texturing [44], and abrasive jet machining [45]) it is now possible to include textures on contact surfaces. Indeed, surface texturing has proved to be very beneficial in the case of hydrodynamic bearing systems [41], where it improves the load-carrying capacity by providing supplementary hydrodynamic pressure [46]; these textures may act as lubricant reservoirs to ensure supply in case of lubricant starvation [47], entrapping wear debris and abrasive particles to prevent severe wear [48] and so reducing friction [49]. The introduction of textures in journal bearings was first initiated by Lu and Khonsari [50], who have presented a series of experimental results to examine the effect of fully and partially textured journal bearings on the Stribeck curve. It was shown that the friction coefficient in fully textured bearing can be reduced, with an appropriate selection of texture size, depth, and density. Tala-Ighil et al. [51,52] investigated the effect of spherical and cylindrical shapes on the performance of the bearings; they used a finite-difference model to solve the two-dimensional Reynolds equation under steady-state conditions by considering Reynolds' boundary condition. It was reported that a textured surface affected the main bearing characteristics. This impact can have either positive or negative influences on this characteristics depending on the dimple parameters (size, depth, density, and distribution). Further, they reported, by means of numerical simulation, that the partial texturing configuration including the texturing of multiple zones has a positive influence on the characteristics of the hydrodynamic contact. Kango et al. [53] performed an investigation related to the combined effects of viscous heat dissipation and non-Newtonian fluid rheology on the performance of textured journal bearings with spherical dimple shape, they used in their investigation the classical Reynolds model and mass conserving algorithm proposed by Elrod and Adams [54]. It was found that JFO boundary conditions provide realistic results compared with those obtained by Reynolds boundary conditions. Recently, Zhang et al. [55] presented a parametric design of texturing surface bearing, with the aim to get the optimal textures distribution and parameters; they reported that the loading capacity of a textured journal bearing may be improved through an appropriate arrangement of textures on the contact surface.

In order to explain the behavior of lubricant inside micro-textured surfaces of mechanical seals, several mechanisms have been proposed. We can cite the following works: the "micro-wedge action" generated by micro-textured features identified by Hamilton et al. [46] and Anno et al. [56]; the "inlet roughness" mechanism proposed by Tønder et al. [57,58]; the "collective dimple effect" proposed by Etsion and Burstein [59]; the "load support mechanism" of inlet suction observed in Olver et al.'s [60] and Fowell et al.'s [61] works; finally, the "balancing wedge action" reported by Yagi and Sugimura [62]. Based on these mechanisms, Nanbu et al. [63] reported that textures with bottom shapes containing a micro-wedge and/or a micro-step bearing mechanisms tend to increase film thicknesses and pressure lift. While, recently, M.S Uddin et al. [64] mentioned that texture shapes with convergent (positive) wedge bottom profile offer the best performance, whereas

divergent (negative) wedge bottom profiles perform the worst. Moreover, they also reported that the dimple shape with micro-step features would be beneficial in reducing friction.

The above-mentioned works show that the tribological performances of textured surfaces are very sensitive to the texture mechanism. Indeed, some dimple shapes with micro-wedge and/or micro-step features perform better by increasing the load lifting capacity and lowering the friction force. The added feature in this study is the combination of the influences of surface texturing (full/partial) and journal misalignment (degree/angle) on the performance of hydrodynamic journal bearings, using Elrod's efficient mass conservation algorithm for implementing the JFO boundary conditions.

This paper is organized as follows. Section 2 provides the description of the modified Reynolds equation, the cavitation boundary condition, the governing equations, and the computational procedure. Section 3 is devoted to numerical results and discussions, and contains the preliminary validation and performance analysis of textured misaligned journal bearings. Finally, our conclusions are given in the last section.

2. Governing equations

2.1. Reynolds equation and Elrod cavitation algorithm

In lubrication theory, the Reynolds equation of thin viscous fluid films is usually used for the prediction of the pressure distribution. For a Newtonian lubricant in a laminar flow with constant viscosity, under the isothermal condition, taking into account assumptions that bushing is stationary and the axial movement of the shaft is neglected, the steady-state Reynolds equation (in Cartesian coordinates) takes the following form:

$$\frac{\partial}{\partial x}\left(\rho h^3 \frac{\partial p}{\partial x}\right) + \frac{\partial}{\partial z}\left(\rho h^3 \frac{\partial p}{\partial z}\right) = 6\mu U \frac{\partial(\rho h)}{\partial x} \tag{1}$$

where p is lubricant pressure, h is film thickness, μ is dynamic viscosity, ρ is lubricant density, and U is the shaft speed in the x direction.

In full-film zone, the density is constant and Eq. (1) becomes:

$$\frac{\partial}{\partial x}\left(h^3 \frac{\partial p}{\partial x}\right) + \frac{\partial}{\partial z}\left(h^3 \frac{\partial p}{\partial z}\right) = 6\mu U \frac{\partial h}{\partial x} \tag{2}$$

In the rupture zone, the pressure remains constant at the cavitation pressure. Hence, Eq. (1) is reduced to:

$$6\mu U \frac{\partial(\rho h)}{\partial x} = 0 \tag{3}$$

In order to take into account the effect of film rupture and reformation, Jakobsson, Floberg [65], and Olsson [66] proposed the so-called JFO boundary conditions. The JFO boundary conditions have been added since they are more realistic than the Reynolds boundary conditions and can consider lubricant cavitation, especially in misaligned [20,22,23], dynamically loaded, and textured bearings [53,67].

To use the JFO boundary conditions, Elrod [54] suggested to combine the two equations (2) and (3) into a single "universal" equation that covers both the cavitated and the full-film regions, by introducing a new parameter called fractional-film content $\Theta = \rho/\rho_c$, where ρ_c is the cavitated oil density.

The resulting mass-conservative form of the Reynolds equation where the unknown is the factional film content instead of the pressure can be written as follows:

$$\frac{\partial}{\partial x}\left(\beta h^3 g \frac{\partial \Theta}{\partial x}\right) + \frac{\partial}{\partial z}\left(\beta h^3 g \frac{\partial \Theta}{\partial z}\right) = 6\mu U \frac{\partial(\Theta h)}{\partial x} \tag{4}$$

where β is the bulk modulus, which represents the variation of the lubricant compressibility in the full-film region, and the pressure p is given by:

$$\beta = \rho \frac{\partial p}{\partial \rho} \tag{5}$$

and $g(\Theta)$ is the switch function (cavitation index), which is zero in the cavitation zone and is equal to unity in the full-film zone.

$$\begin{cases} g = 1 & \text{if} \quad \Theta \geq 1 \\ g = 0 & \text{if} \quad \Theta < 1 \end{cases} \tag{6}$$

After solving Eq. (4) for Θ, the pressure in the full-film region can be determined using the following relation [54]:

$$p = p_c + \beta g \ln(\Theta) \tag{7}$$

where p_c is the cavitation pressure.

By introducing the following dimensionless parameters:

$$\theta = x/R \qquad Z = z/L \qquad \overline{h} = h/C \qquad \overline{y} = y/h \qquad \overline{\beta} = \frac{\beta C^2}{\mu U R}$$

where R is the bearing's radius, L is the bearing's length, and C is radial clearance.

The dimensionless form of the modified Reynolds equation becomes:

$$\frac{1}{12}\frac{\partial}{\partial\theta}\left(\overline{\beta}\, g\, \overline{h}^3 \frac{\partial \Theta}{\partial\theta}\right) + \left(\frac{R}{L}\right)^2 \frac{1}{12}\frac{\partial}{\partial Z}\left(\overline{\beta}\, g\, \overline{h}^3 \frac{\partial \Theta}{\partial Z}\right) = \frac{1}{2}\frac{\partial(\Theta\overline{h})}{\partial\theta} \tag{8}$$

and the dimensionless pressure is described by:

$$\overline{P} = \overline{P}_c + \overline{\beta}\, g\, \ln(\Theta) \tag{9}$$

2.2. Film thickness

The oil film's thickness h is the gap between the journal and the bushing, filled with a liquid lubricant, which generates the required hydrodynamic pressure. It is one of the most important parameters in the Reynolds equation, which needs to be carefully considered in the analysis. Therefore, the Reynolds equation should be modified to allow film thickness to be varied in both directions, taking into account the combined effect of bearing surface texturing and shaft misalignment.

1. Smooth misaligned journal bearing

   In the case of general misaligned conditions, the approach taken from Maspeyrot and Frene's [68] paper is used to represent the oil film thickness distribution inside the bearing with provision for misalignment in both circumferential and axial directions, as shown in Fig. 1.

$$h_{(\theta,z)} = C + e_0\,(1 + \cos(\theta)) + e'\left(\frac{z}{L} - \frac{1}{2}\right)\cos(\theta - \alpha) \tag{10}$$

   where e_0 is the eccentricity at the bearing mid-plane, e' is the magnitude of the projected journal axis on the bearing mid-plane, α is the misalignment angle between the line of centers and the rear center of the misaligned journal (see Fig. 1).

   The dimensionless film thickness is described by:

$$\overline{h}_{(\theta,\overline{Z})} = (1 + \varepsilon\cos(\theta)) + \varepsilon'\left(\overline{Z} - \frac{1}{2}\right)\cos(\theta - \alpha) \tag{11}$$

   the parameters ε is the eccentricity ratio at the bearing mid-plane ($\varepsilon = e_0/C$) and ε' is the misalignment eccentricity ratio, which represents the magnitude of the projection of the complete journal center line on the mid plane, and can be computed from [20]

$$\varepsilon' = \frac{e'}{C} = D_m\, \varepsilon'_{max} \tag{12}$$

   where D_m is the dimensionless degree of misalignment (values from 0 to 1) and ε'_{max}, the maximum possible value of ε', is given by:

$$\varepsilon'_{max} = 2\left(\sqrt{1 - \varepsilon^2\,\sin^2(\alpha)} - \varepsilon\,|\cos(\alpha)|\right) \tag{13}$$

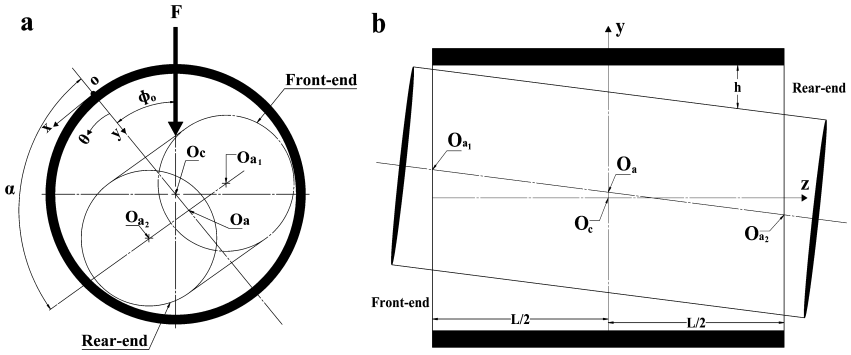

Fig. 1. Representative scheme of a misaligned journal bearing.

2. Textured misaligned journal bearing

The normalized lubricant film thickness in the case of a textured misaligned journal bearing is described by a function of the form:

$$\overline{h}_{T_{(\theta,\overline{Z})}} = \overline{h}_{(\theta,\overline{Z})} + \overline{\Delta h}_{(\theta,\overline{Z})} \tag{14}$$

where $\overline{h}_{(\theta,\overline{Z})}$ denotes the smooth part (without textures equation (11)) of the film geometry and $\overline{\Delta h}_{(\theta,\overline{Z})}$ is the film thickness variation due to the dimple surface; it characterizes the depth of the fluid film in the texture (Fig. 2).

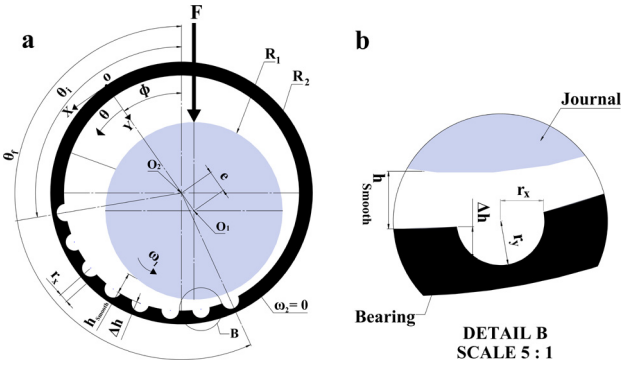

Fig. 2. Representative scheme of a journal bearing: (a) a straight section of the textured journal bearing; (b) detailed section for the texture scheme.

2.3. Texture shapes and geometries

In general, textures can be characterized by their shape (contour geometry, bottom profile), size (contour dimension, depth), number (along axial/circumferential directions), density, and distribution. Zhang et al. [69] reported that the square texture shape performed the best hydrodynamic enhancement, followed by the triangle, the circle, and the rectangle. According to that reasoning, in this study, three texture shapes are adopted: square, cylindrical, and triangular to highlight its effect on the particular case of journal bearings. Table 1 summarizes the texture geometries, parameters, and equations. The coordinates of the texture center C are noted $(x_c,\ y_c\,,z_c)$. This center is located on the bearing surface, making $y_c = 0$. The depth of any point located on the texture geometry is given by $\Delta h_{(x,z)}$. The texture dimensional parameters in the x, y, and z directions are r_x, r_y, and r_z, respectively.

Table 1
Geometric parameters and equations for the studied texture shapes.

Description	Square "SQ"	Cylinder "CY"	Triangle "TR"
Texture shapes	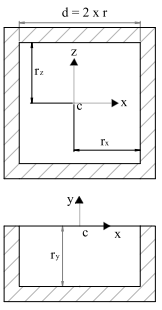	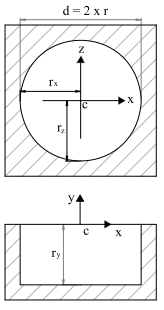	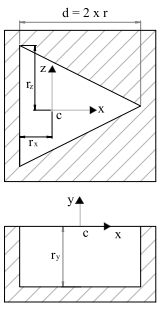
Geometric equations	if $\begin{cases} -r_x \le x \le r_x \\ -r_z \le z \le r_z \end{cases}$ $\Delta h\,(x,z) = r_y$	if $\begin{cases} r_x = r_z = r \\ (x-x_c)^2 + (z-z_c)^2 = r^2 \end{cases}$	if $\begin{cases} -r_x \le x \le r_x \\ \frac{r_z}{2r_x}x \le z \le -\frac{r_z}{2r_x}x + r_z \end{cases}$

De-Kraker et al. [70] reported that the ratio S between the film thickness $h_{\min}$ and the dimple depth r_y is the key texture parameter; they demonstrated that the Reynolds equation can be used to investigate the effects of texture when a ratio $S < 1$ exists. According to that reasoning, the following shape dimensions are chosen: $r_x = r_z = 3$ mm and $r_y = 0.025$ mm, where $S = 0.8$.

Tala-Ighil et al. [52] simulated 25 cases of cylindrical texture shape with different texture distributions, including full texturing and partial texturing with one or multiple separated zones of the bearing surface. They reported that, on one side, full texturing has a detrimental effect, and partial texturing, on the other side, has a positive influence. Furthermore, they reported that the optimal region where texturing can provide more efficiency is located at the second half of bearing surface, (beyond 180°), at the declining part of the pressure field. Due to this, two texture configurations, as shown in Fig. 3, are considered herein for exploration.

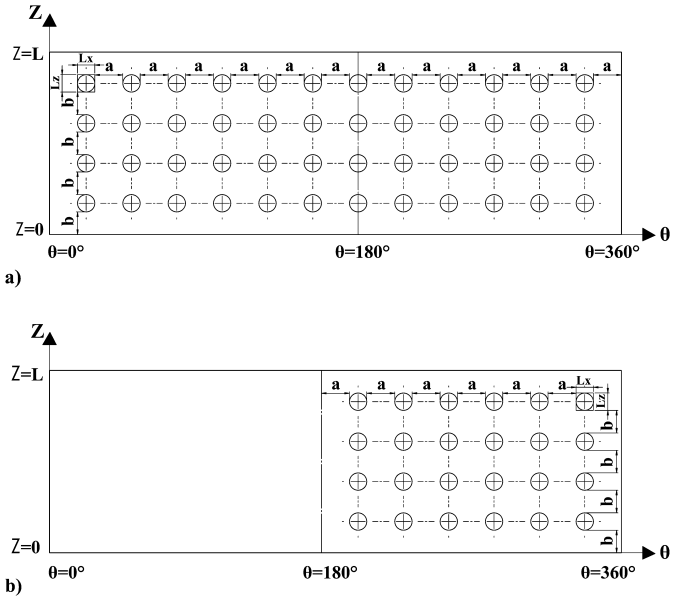

Fig. 3. Illustration of the texture distribution in the circumferential and axial directions on the bearing surface: (a) fully textured cases (from 0° to 360°); (b) partially textured cases (from 180° to 360°).

2.4. Computational procedure

Based on the mass conservation algorithm (JFO boundary conditions), the approach proposed by Vijayaraghavan and Keith [71] is used herein. The finite differences method with Gauss–Seidel's iterative process (successive over-relaxation "SOR") is employed to compute the fractional film content (Θ). Usually, an iterative loop with a convergence criterion is required when JFO boundary conditions are imposed [67]. Moreover, this method is very easy to implement, which makes it the preferred solver for small and medium-sized problems [72]. In order to improve the convergence speed and avoid the problem in stabilizing the cavitation zone, the modified switch function algorithm developed by Fesanghary and Khonsari [72] is used in the computational code, where the "gfactor" is chosen in the range from 0 to 0.9.

The computational process consists of the following steps:

- introduction of input data: L/D, ε, D_{m} and α;
- input initial values of the fractional film content $\Theta^0_{(\theta,Z)}$, the binary switch function $g^0_{(\theta,Z)}$, and the film thickness $h^0_{(\theta,Z)}$;
- resolution of the modified Reynolds equation (4);
- imposition of boundary conditions on the affected nodes (JFO condition);
- obtaining the fractional film content by verifying the following convergence condition: $\dfrac{|\Delta\Theta_{i,j}|}{\Theta_{i,j}} \leq tol_{\Theta}$ at each node (i, j) of the bearing surface mesh.
- determination of the pressure profile, once the convergence condition is satisfied, using Eq. (7) and deduction of the bearing's characteristics.

The process described above corresponds to the resolution of a direct problem whose eccentricity ratio ε, D_{m} and α values are known, for the inverse problem that consist in the determination of the position (the relative position ε, the degree D_{m}, and the misalignment angle α) of the journal in the bearing for imposed applied load $\overline{F}$ and moment (magnitude $\overline{M}$ and direction ϕ_{M}).

The procedure consists of the following steps:

- input initial values of the eccentricity ratio ε_0, the degree D_{m_0}, and the angle α_0 of misalignment;
- solving the direct problem for the values of ε_0, D_{m_0}, and α_0;

- the calculated load-carrying capacity $\overline{W}_{\mathrm{C}}$ is compared with the applied load $\overline{F}$; the calculated misalignment direction $\phi_{M_{\mathrm{C}}}$ is compared with the applied moment direction ϕ_{M} and the calculated misalignment moment $\overline{M}_{\mathrm{C}}$ is compared with the applied moment $\overline{M}$;
- calculating a new eccentricity ratio ε, a new angle of misalignment α, and a new degree of misalignment D_{m} by the method of Brent [73];
- stopping the process after the load convergence condition $\dfrac{|\overline{W}_{\mathrm{C}} - \overline{F}|}{\overline{F}} \leq tol_{\mathrm{W}}$ is achieved; the misalignment angle convergence criteria $|\phi_{M_{\mathrm{C}}} - \phi_{\mathrm{M}}| \leq tol_{\phi_{\mathrm{M}}}$ and the moment convergence condition $\dfrac{|\overline{M}_{\mathrm{C}} - \overline{M}|}{\overline{M}} \leq tol_{\mathrm{M}}$ are satisfied.

We present the global computational procedure in the flowchart in Fig. 4.

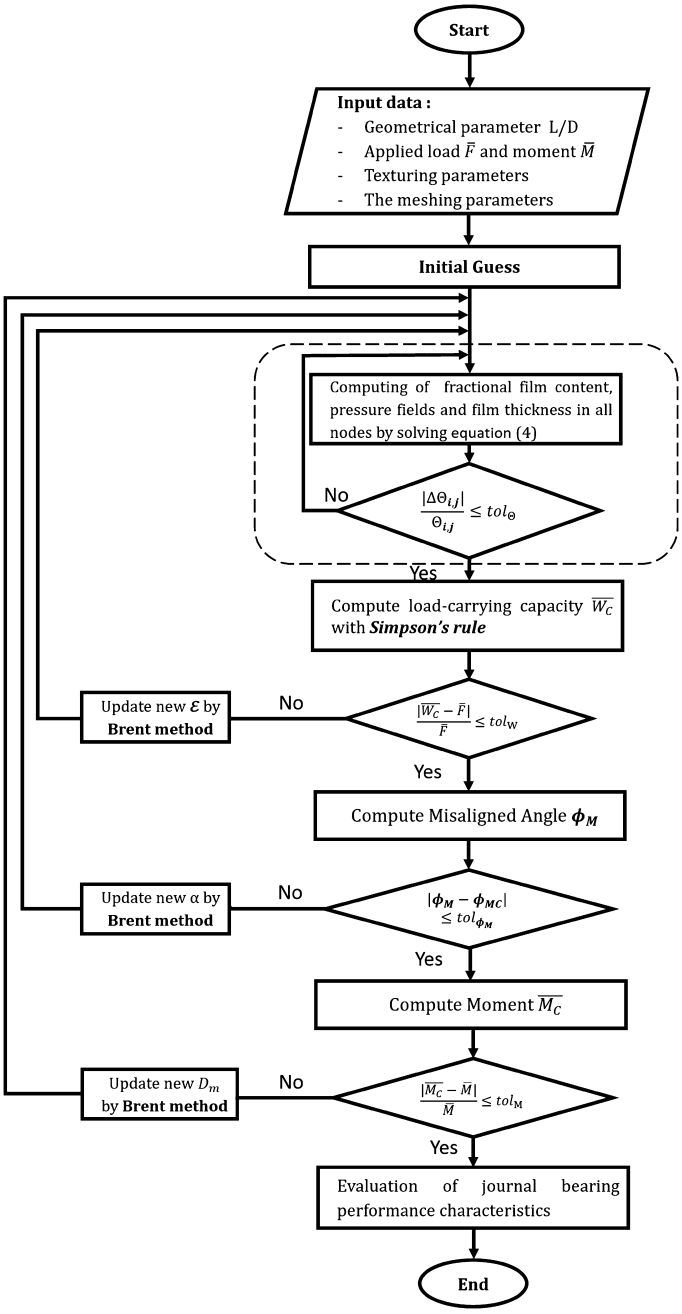

Fig. 4. Flowchart of the global computational procedure.

2.5. Miscellaneous parameters

The performance characteristics of misaligned journal bearing for smooth/textured cases are computed using the relations below.

The dimensionless load components in the circumferential and the axial directions are given by:

$$\begin{cases} \overline{W}_\theta = -\int_0^1 \int_0^{2\pi} \overline{P}\cos(\theta)\,\mathrm{d}\theta\,\mathrm{d}Z \\ \overline{W}_Z = \int_0^1 \int_0^{2\pi} \overline{P}\sin(\theta)\,\mathrm{d}\theta\,\mathrm{d}Z \end{cases} \tag{15}$$

Then the total bearing load capacity and the attitude angle are:

$$\begin{aligned} \overline{W}_\mathrm{C} &= \sqrt{\overline{W}_\theta^2 + \overline{W}_Z^2} \\ \phi &= \arctan\left(\frac{\overline{W}_\theta}{\overline{W}_Z}\right) \end{aligned} \tag{16}$$

The dimensionless leakage flow rate through the ends of the bearing, noted $\overline{Q}_1$ from the left-hand bearing end and $\overline{Q}_2$ from the right-hand bearing end, are given by:

$$\begin{cases} \overline{Q}_1 = -\int_0^1 \int_0^{2\pi} \frac{1}{2}\frac{\partial \overline{P}}{\partial Z}\bar{h}^3\,\bar{y}\,(\bar{y}-1)\,\mathrm{d}\theta\mathrm{d}\bar{y} \quad \textit{for}: Z=0 \\ \overline{Q}_2 = \int_0^1 \int_0^{2\pi} \frac{1}{2}\frac{\partial \overline{P}}{\partial Z}\bar{h}^3\,\bar{y}\,(\bar{y}-1)\,\mathrm{d}\theta\mathrm{d}\bar{y} \quad \textit{for}: Z=1 \end{cases} \tag{17}$$

then the total end lubricant flow rate is

$$\overline{Q}_Z = \left|\overline{Q}_1\right| + \left|\overline{Q}_2\right| \tag{18}$$

The dimensionless friction force acting on the journal's surface is given by:

$$\overline{F}_t = \int_0^1 \int_0^{\theta_S} \frac{1}{2}\frac{\partial \bar{P}}{\partial \theta}\bar{h}\,\mathrm{d}\theta\,\mathrm{d}Z + \int_0^1 \int_0^{\theta_S} \frac{1}{\bar{h}}\,\mathrm{d}\theta\,\mathrm{d}Z + \int_0^1 \int_{\theta_S}^{2\pi} \frac{\overline{h}_s}{\overline{h}^2}\,\mathrm{d}\theta\mathrm{d}Z \tag{19}$$

where θ_s is the angular coordinate at the starting cavitation zone and $\overline{h}_s$ is the equivalent of the oil film thickness in the cavitation zone.

Consequently, the frictional coefficient is obtained as follows:

$$f\left(\frac{R}{C}\right) = \frac{\overline{F}_t}{\overline{W}} \tag{20}$$

Under misalignment, the bearing pressure is not symmetric to its mid-plane and it will make some misaligned moments to act on the journal. Two dimensionless components of the moment, circumferential and axial, can be written as follows:

$$\begin{cases} \overline{M}_\theta = \int_0^1 \int_0^{2\pi} \overline{P}\,(Z-0.5)\,\sin\theta\,\mathrm{d}\theta\,\mathrm{d}Z \\ \overline{M}_Z = \int_0^1 \int_0^{2\pi} \overline{P}\,(Z-0.5)\,\cos\theta\,\mathrm{d}\theta\,\mathrm{d}Z \end{cases} \tag{21}$$

then the total misalignment moment and its direction angle are:

$$\overline{M} = \sqrt{\overline{M}_\theta^2 + \overline{M}_Z^2} \tag{22}$$

$$\phi_{\mathrm{M}} = \arctan\left(-\frac{\overline{M}_\theta}{\overline{M}_Z}\right) \tag{23}$$

All numerical integrations was carried-out by means of Simpson's rule.

3. Numerical results and discussions

3.1. Preliminary validation

Based on the analysis described in the present paper, a MATLAB computer program was developed. This section is devoted to the validation of our computational code. To this end, a comparison analysis is performed between the results of the present analysis and those from research works [22,23,52] for aligned/misaligned journal bearings with smooth/textured surfaces.

Case 1: Misaligned journal bearing with smooth surface

1. Comparison with experimental results
   Bouyer and Fillon [22] performed experimental measurements in a misaligned journal bearing, and showed the maximum pressure in the mid-plane and the minimum film thickness as a function of misaligned moment at a fixed bearing load. Fig. 5 shows the comparison between the present predicted results and those carried out by Bouyer and Fillon [22]. As the bearing is aligned, the moment is nil. When the moment increases, the maximum pressure and the minimum film thickness decrease. The results of the present comparison are in good agreement with those of the already mentioned paper [22]. It should be emphasized that the predicted results are slightly higher than those measured experimentally. The noticed differences are most probably due to the adopted assumptions: negligible cavitation pressure, Newtonian fluid in isothermal regime ($T = 40\,^\circ$C).
   The two-dimensional results of film thickness, fractional-film content, and pressure distributions obtained by the computational code are plotted in Figs. 6 and 7, for aligned (case $M = 0$ N·m) and misaligned (case $M = 50$ N·m) journal bearings, respectively, in order to further check its validity. In Fig. 6, the film thickness evolution remains constant in the axial direction, and its minimum value occurs near $\theta = 181^\circ$. In a fractional-film content distribution, the area where $\Theta \geq 1$ represents the full film region, and the area where $\Theta \leq 1$ represents the cavitation region; the variation in the fractional film content in the full film region is very small due to the large bulk modulus, while in the cavitation region, it drops significantly to $\Theta = 0.4$. However, a small variation in the fractional film content in the full film region causes a large change in the pressure distribution, as a result of the large value of the compressibility. Due to the atmospheric pressure imposed on the axial boundary, the fractional film content at $z = 0$ and $z = L$ is assumed to be $\Theta = 1$, while on the circumferential boundary it is due to the bearing oil supply conditions. The simulations also show the pressure distribution for aligned bearings, where the maximum pressure occurs near $\theta = 138^\circ$ in the bearing mid-plane $z = L/2$. The influence of misalignment is shown very clearly in Fig. 7. The minimum film thickness occurs near $\theta = 140^\circ$ on the rear end $z = 0$ and near $\theta = 265^\circ$ on the front end $z = L$. The variation in the fractional film content in the axial direction is very severe, and the cavitation region begins after the minimum film thickness and disappears in the bearing groove. Moreover, the boundary between the full film and the rupture regions is twisted severely, as a result of a variation in axial minimum film thickness locations. The maximum pressure location is shifted to the rear end, $z = 0$, and its value is greater compared to the aligned bearing. The highest pressure at each axial location occurs before the minimum film thickness, and its direction is roughly matching with the direction of the minimum film thickness.

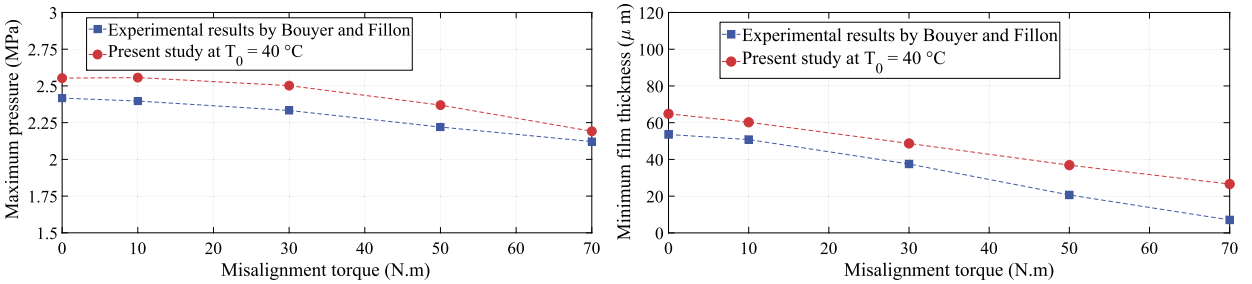

Input data:						
	$F = 9000$ (N)	$N = 4000$ (rpm)	$p_a = 0.08$ (MPa)	$\mu = 0.0293$ (Pa·s)	$T_0 = 40\,^\circ$C	$\phi_{\mathrm{M}} = 0^\circ$
	$L = 80$ (mm)	$D = 99.78$ (mm)	$C = 117.5$ (μm)	$l_{\mathrm{G}} = 70$ (mm)	$\psi_{\mathrm{G}} = 0^\circ$	$\Delta\psi_{\mathrm{G}} = 18^\circ$

Fig. 5. Comparison between the results of the present study and those of Bouyer and Fillon's experiments [22].

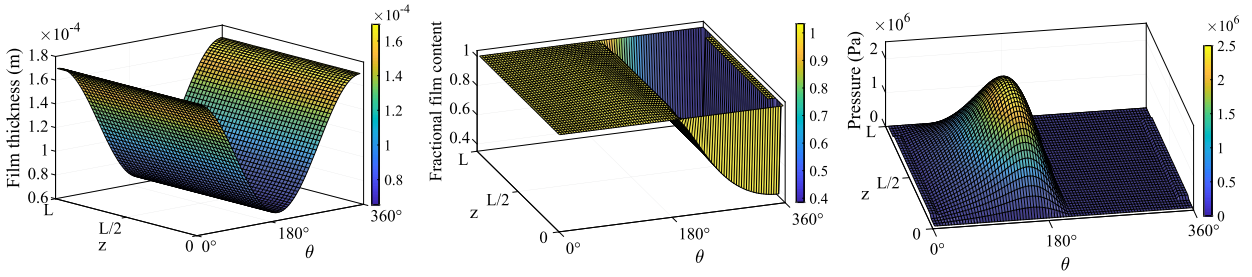

Fig. 6. Film thickness evolution, fractional-film content and pressure distributions on the contact in an aligned journal bearing (case $M = 0$ N·m).

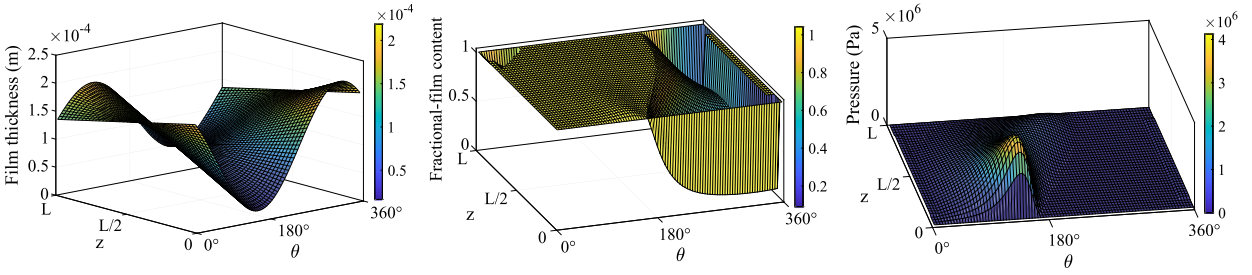

Fig. 7. Film thickness evolution, fractional film content and pressure distributions on the contact in a misaligned journal bearing (case $M = 50$ N·m).

2. Comparison with numerical results
   Here, a comparison analysis is performed between our results and those computed by Jang and Khonsari [23], for aligned/misaligned journal bearings with smooth surfaces.
   Parameters adopted for this comparison are:
   - bearing data: (a) amplitude of external load $F = 20\,000$ N; (b) amplitude of applied moment $M = 0$ or 76 N·m; (c) applied moment direction $\phi_M = 224.5°$; (d) journal diameter $D = 0.040$ m; (e) bearing length $L = 0.080$ m; (f) radial clearance $C = 0.00003$ m; (j) rotational speed $N = 2500$ rpm; (h) lubricant viscosity $\mu = 0.02$ Pa·s; (i) bulk modulus $\beta = 5$ GPa;
   - computational method parameters: (a) finite-difference method (FDM) with JFO boundary conditions; (b) grid size (91, 41); (c) convergence criteria $tol_\Theta = 10^{-6}$, $tol_W = 10^{-4}$, $tol_M = 10^{-3}$, $tol_{\phi_M} = 10^{-2}$.

   Table 2 presents the comparison between our predictions and those of the already mentioned paper [23]. It can be noted that the obtained values are very close to the reference ones with slight differences that may be due to the computational errors in the simulation.

Table 2
Comparison of the performance characteristics of aligned/misaligned journal bearings.

		Present study		Jang and Khonsari [23]	
Imposed misalignment torque	M (N·m)	0	76	0	76
Eccentricity ratio	ε	0.395	0.373	0.392	0.378
Degree of misalignment	D_m	–	0.500	–	0.53
Angle on misalignment	α	–	121°	–	–
Maximum pressure	P_{max} (MPa)	5.799	6.976	5.90	6.81
Leakage flow rate	Q (cm^3/s)	3.153	3.702	2.9	3.1
Attitude angle	ϕ (°)	67.618	65.616	69.1	68.0
Friction coefficient	f	0.0037	0.0039	0.0039	0.0040

Case 2: Textured journal bearing

In order to develop more confidence in the developed computer program, a comparison analysis is performed between our results and those of Tala-Ighil et al. [52] for textured journal bearings with cylindrical dimple shape.

- The parameters adopted for this case are:
  - bearing data: (a) amplitude of external load $F = 12\,600$ N; (b) journal diameter $D = 0.063$ m; (c) bearing length $L = 0.063$ m; (d) radial clearance $C = 0.00003$ m; (e) angular speed $\omega_1 = 625.4$ rad/s; (f) lubricant viscosity $\mu = 0.0035$ Pa·s;
  - bearing texture data: (a) cylindrical texture shape (b) texture radius $r_x = r_z = 1$ mm; (c) texture depth $r_y = 0.015$ mm;

- computational parameters: number of nodes per texture along the circumferential $nN_{t\,\theta} = 10$ and axial $nN_{t\,Z} = 10$ directions;
- computational method parameters: (a) finite-difference method (FDM) with Reynolds boundary conditions; (b) grid size (891, 142); (c) convergence criteria $tol_{\mathrm{p}} = 10^{-4}$ and $tol_{\mathrm{W}} = 10^{-5}$.

Unlike in Tala-Ighil et al.'s [52] work, Simpson's rule was used to compute all numerical integrations and the Brent method [73] for the estimation of the new eccentricity ratio ε in the convergence loop.

The comparison results are presented in Table 3. The results of the present comparison are in good agreement, with one slight difference, which is due to the choice made concerning the numerical integration method.

In order to further show the effectiveness of our computational code, Figs. 8 and 9 present the prediction results for the film thickness and the pressure profile for smooth, fully, and partially textured cases. The results present in these

Table 3
Comparison of performance characteristics of smooth/textured aligned journal bearings.

		Present study			Tala-Ighil et al. [52]		
		Smooth	Fully textured	Partially textured	Smooth	Fully textured	Partially textured
Eccentricity ratio	ε	0.6010	0.6995	0.5992	0.601	0.709	0.595
Minimum film thickness	$h_{\min}$ (μm)	11.969	9.0145	12.0245	11.97	8.71	12.16
Maximum pressure	$P_{\max}$ (MPa)	7.673	8.191	7.591	7.71	8.26	7.58
Attitude angle	ϕ (°)	50.380	46.151	49.05	50.5	46.1	49.3
Axial flow	$Q \times 10^{-5}$ (m^3/s)	1.723	1.412	1.714	1.743	1.422	1.733

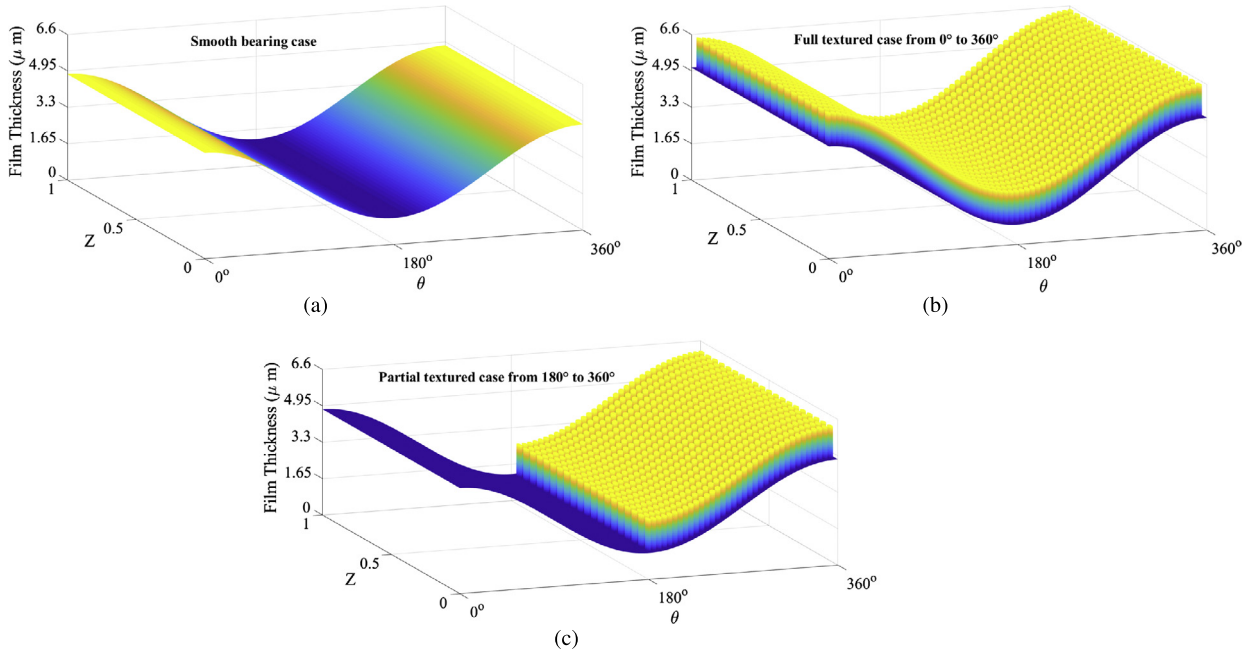

Fig. 8. Film thickness evolution on the contact for smooth/textured journal bearings.

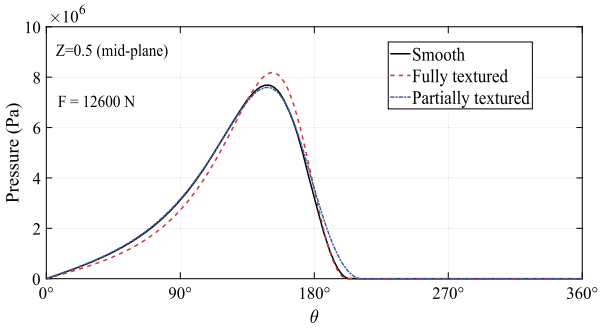

Fig. 9. Pressure profile on the contact along the circumferential direction at bearing mid-plane for smooth/textured journal bearing cases.

figures show very clearly the influence of textures on film thickness evolution and pressure profile, when compared to the smooth surface bearing case.

3.2. Performance analysis of textured misaligned journal bearing

In this section, our objective is to point out the preponderant effect (in terms of tribological properties) between bearing texture surface and journal misalignment. To achieve this end, a series of obtained results for smooth/textured bearing cases are presented to investigate the effect of the misalignment degree and angle on the performances of fully and partially textured journal bearings through three texture shapes (square "SQ", cylindrical "CY" and triangular "TR").

The geometrical characteristics of the bearings, as well as the texturing parameters are given in Table 4.

Table 4
Geometrical and texturing parameters for the studied journal bearing.

Geometrical parameters			Dimensionless variables	
Shaft diameter	D (mm)	40		
Bearing length	L (mm)	40	L/D	1
Radial clearance	C (μm)	50		
Eccentricity ratio	e (μm)	30	e/C	0.6
Texturing parameters				
Texture diameter	d_x (mm)	6	$\overline{d}_x = d_x/R$	0.3
Texture length	d_z (mm)	6	$\overline{d}_z = d_z/L$	0.15
Texture depth	r_y (μm)	25	$\overline{r}_y = r_y/C$	0.5
Texture number along the circumference	nC_θ		Full textured: 16	Partial textured: 8
Texture number along the length	nC_z		5	
Operating conditions				
Journal speed	N (rpm)	3000		
Viscosity	μ (Pa·s)	0.05		
Bulk modulus	β (MPa)	100	40	
Grid size and convergence criteria				
Nodes per texture along the circumference	nN_{tx}		15	
Nodes per texture along the length	nN_{tz}		13	
Nodes in circumferential direction	nN_θ		421	
Nodes in axial direction	nN_z		121	
Nodes across the fluid film	nN_y		121	
Convergence criteria	tol_Θ		10^{-8}	

Figs. 10 and 11 show the 3D representations of the textured bearings. Note that the bearing is with a line groove of negligible thickness, situated at the maximum film thickness and extending at the bearing's ends.

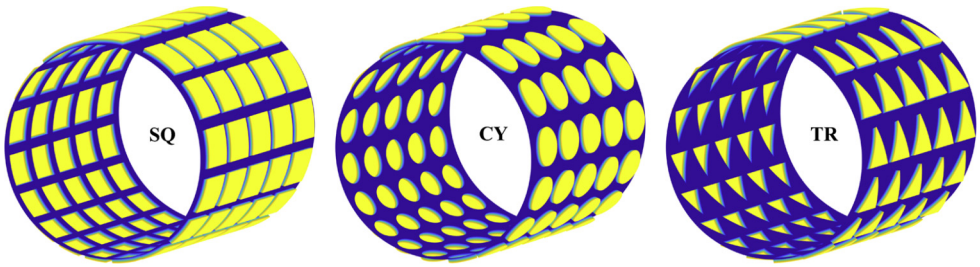

Fig. 10. Geometrical representation of a full textured bearing "0° to 360°" (square (left), cylinder (middle), and triangle (right)).

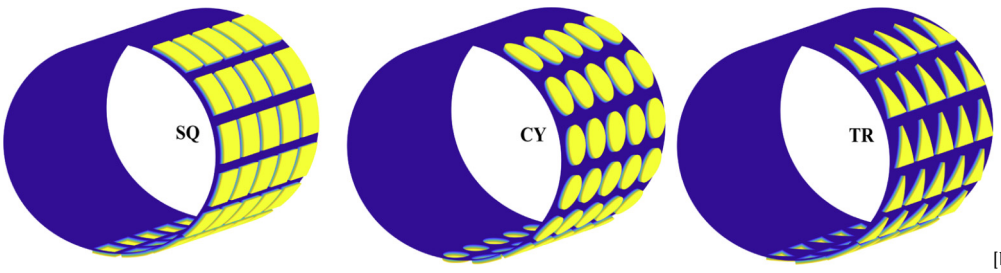

[b]

Fig. 11. Geometrical representation of a partial textured bearing "180° to 360°" (square (left), cylinder (middle), and triangle. (right)).

3.2.1. Textured aligned/misaligned journal bearing: 2D versus 3D simulations

In order to examine the validity of the three-dimensional 3D and two-dimensional 2D analysis of the developed computational code, we provide benchmark results for smooth and full/partial textured aligned ($D_m = 0$) and misaligned ($D_m = 0.75$) journal bearings.

Figs. 12, 13, 14 and 15 show the three-dimensional 3D distribution of the thickness of a lubricant film computed at the contact interface for smooth, fully, and partially textured bearings with square texture shape. In Fig. 12, the bearing

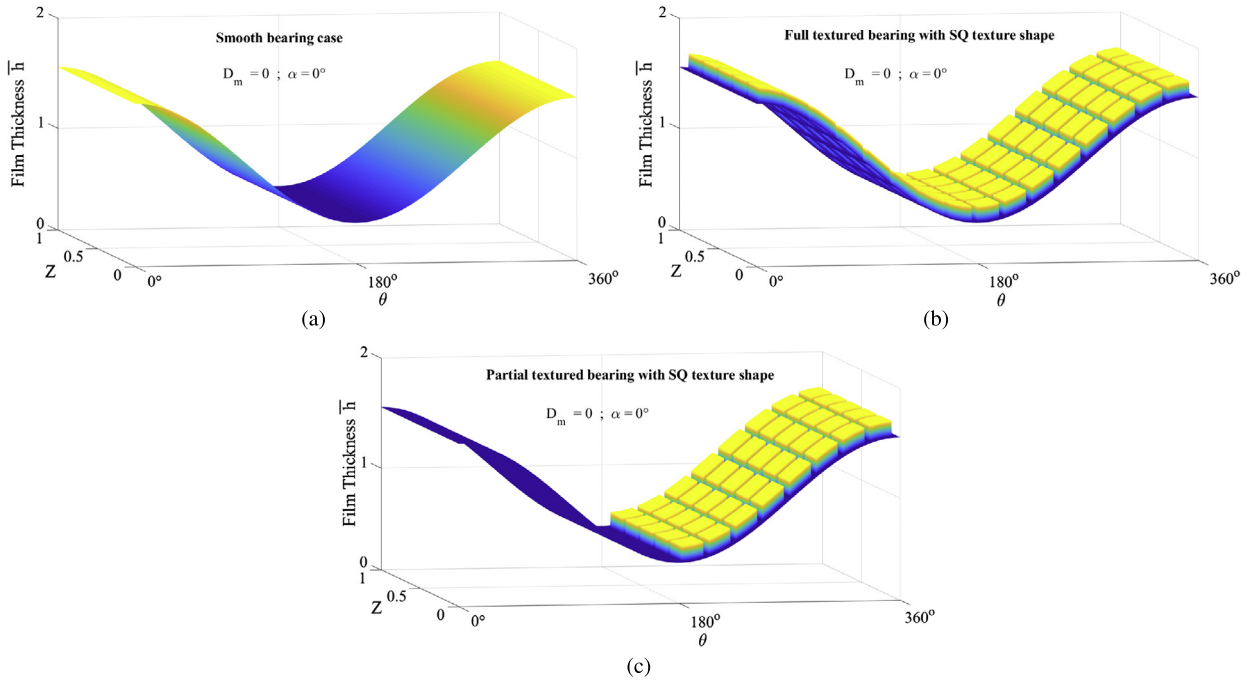

Fig. 12. Evolution of dimensionless film thickness versus axial and circumferential coordinates for an aligned journal bearing: (a) smooth bearing; (b) fully textured bearing (from 0° to 360°); (c) partially textured bearing (from 180° to 360°).

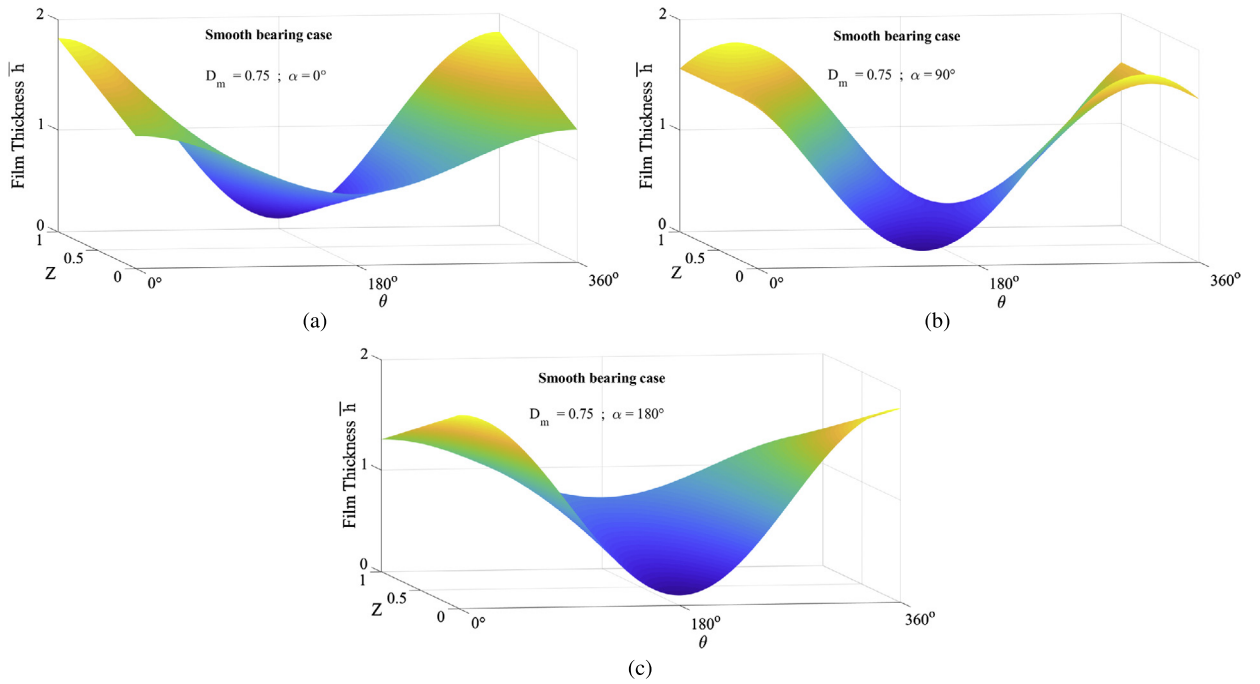

Fig. 13. Evolution of smooth dimensionless film thickness versus axial and circumferential coordinates for a misaligned journal bearing: (a) $\alpha = 0°$; (b) $\alpha = 90°$; (c) $\alpha = 180°$.

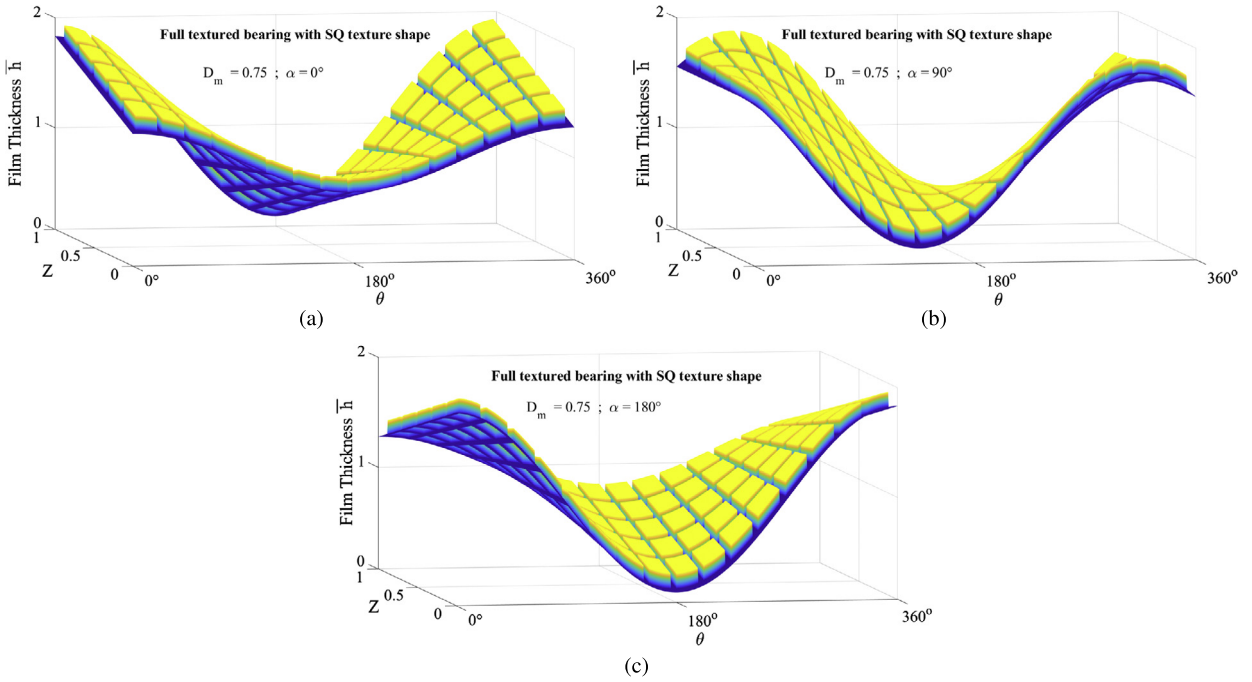

Fig. 14. Evolution of fully textured dimensionless film thickness versus axial and circumferential coordinates for a misaligned journal bearing: (a) $\alpha = 0°$; (b) $\alpha = 90°$; (c) $\alpha = 180°$.

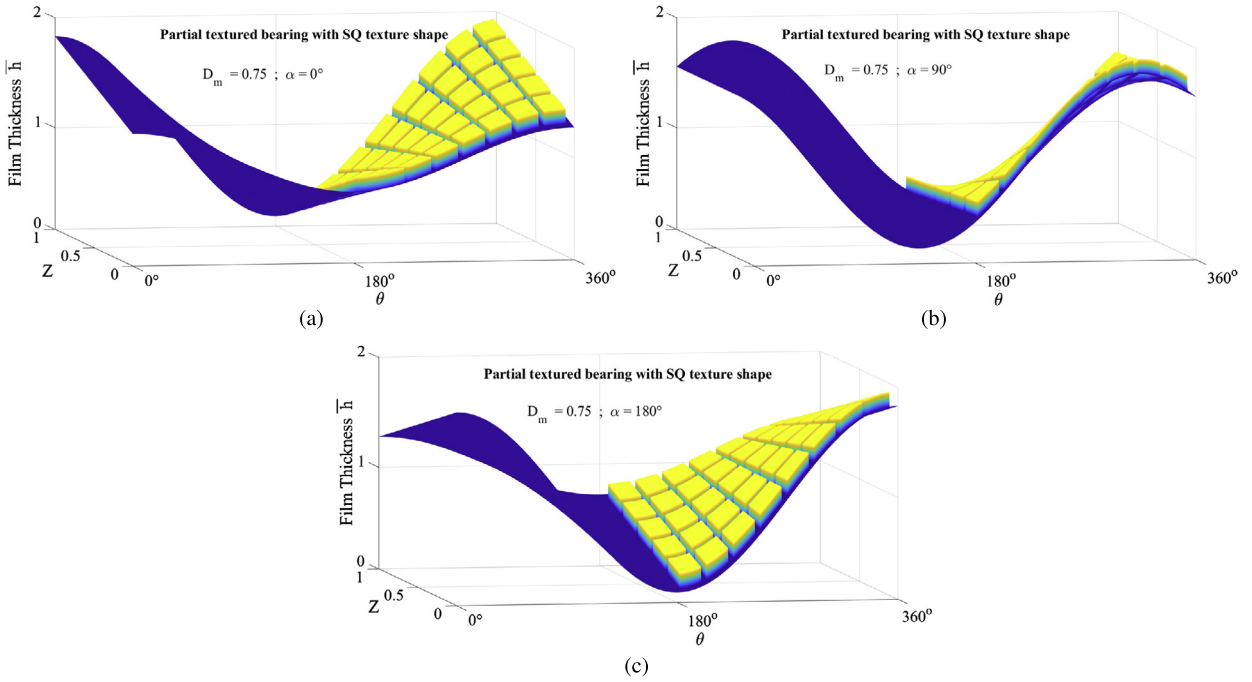

Fig. 15. Evolution of partially textured dimensionless film thickness versus axial and circumferential coordinates for a misaligned journal bearing: (a) $\alpha = 0°$; (b) $\alpha = 90°$; (c) $\alpha = 180°$.

is aligned, film thickness evolution for smooth (Fig. 12a), fully textured (Fig. 12b), and partially textured (Fig. 12c) surface bearings remain constant in the axial direction, and its minimum value occurs near $\theta = 181°$. As the bearing is misaligned, film thickness evolution for smooth (Fig. 13), fully textured (Fig. 14), and partially textured (Fig. 15) surface bearings is plotted for three values of the misalignment angle: (a) $\alpha = 0°$, (b) $\alpha = 90°$ and (c) $\alpha = 180°$. Compared to the aligned bearing, the minimum film thickness value occurs near $\theta = 181°$, on the rear end ($z = 0$) for $\alpha = 0°$ (Figs. 13a, 14a and

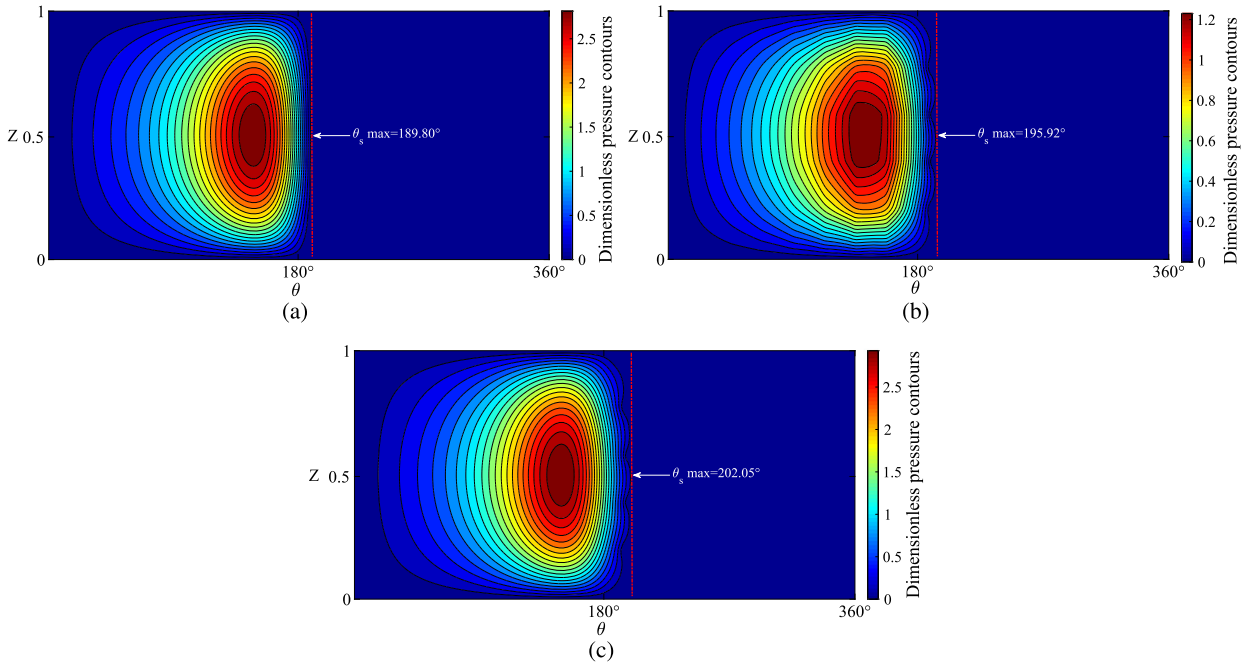

Fig. 16. Distribution of dimensionless pressure versus axial and circumferential coordinates for an aligned journal bearing: (a) smooth bearing; (b) fully textured bearing (from 0° to 360°); (c) partially textured bearing (from 180° to 360°).

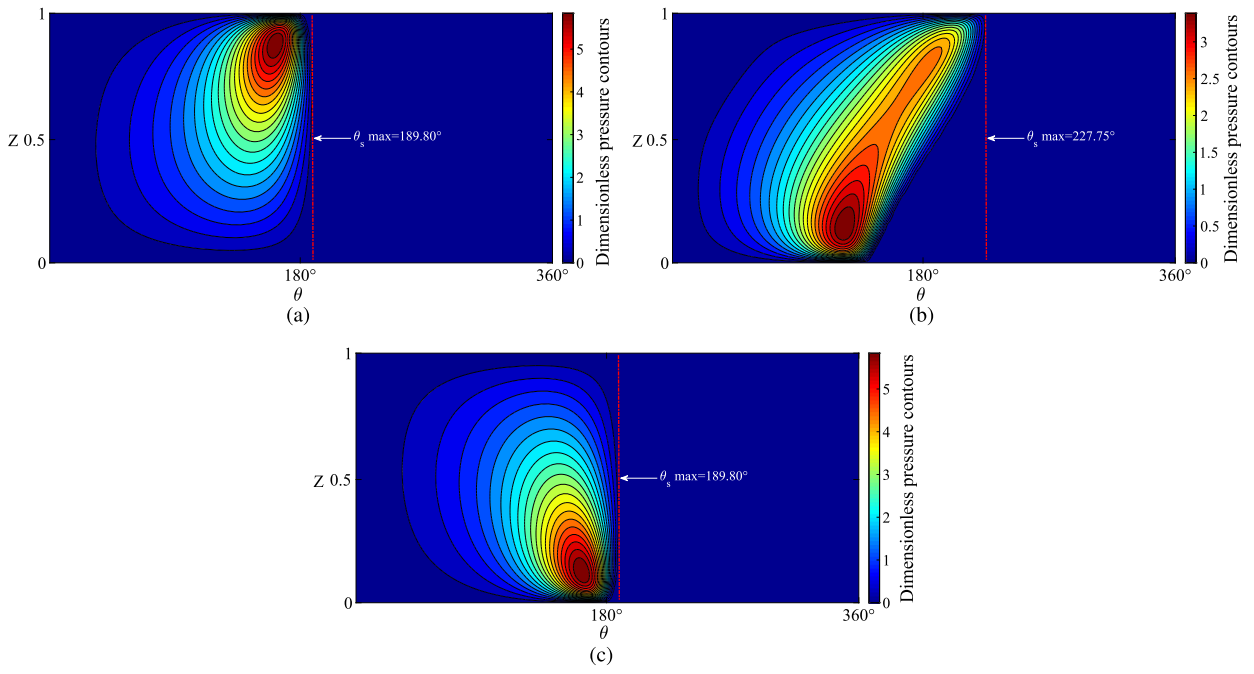

Fig. 17. Distribution of smooth dimensionless pressure versus axial and circumferential coordinates for a misaligned journal bearing: (a) $\alpha = 0°$; (b) $\alpha = 90°$; (c) $\alpha = 180°$.

15a), and on the front end ($z = L$) for $\alpha = 180°$ (Figs. 13b, 14b and 15b), whereas, in the case when $\alpha = 90°$, the minimum film thickness occurs for two values, near $\theta = 140°$ on the rear end and near $\theta = 230°$ on the front end (Figs. 13c, 14c and 15c).

The variations in the dimensionless pressure distribution for smooth/textured surface aligned/misaligned journal bearings are shown in Figs. 16, 17, 18 and 19. As the bearing is aligned (Fig. 16), in the smooth bearing case (Fig. 16a), the dimensionless maximum pressure location occurs near $\theta = 147.66°$ in the bearing mid-plane $z = L/2$, with the value of

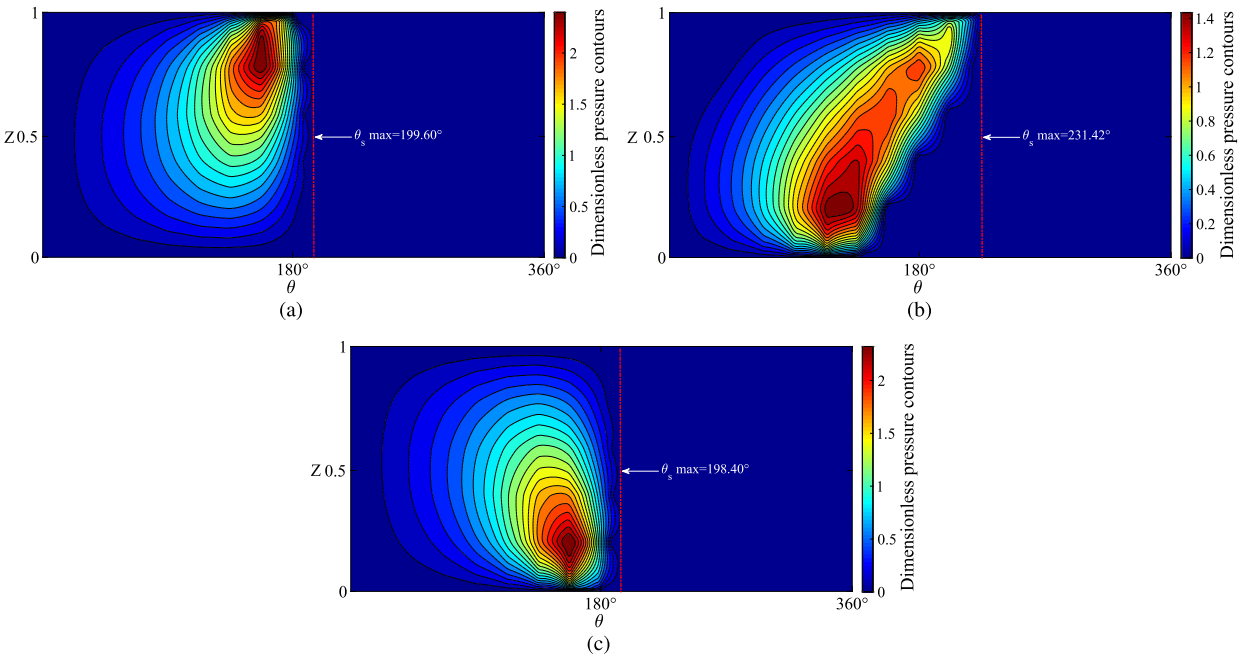

Fig. 18. Distribution of fully textured dimensionless pressure versus axial and circumferential coordinates for a misaligned journal bearing: (a) $\alpha = 0°$; (b) $\alpha = 90°$; (c) $\alpha = 180°$.

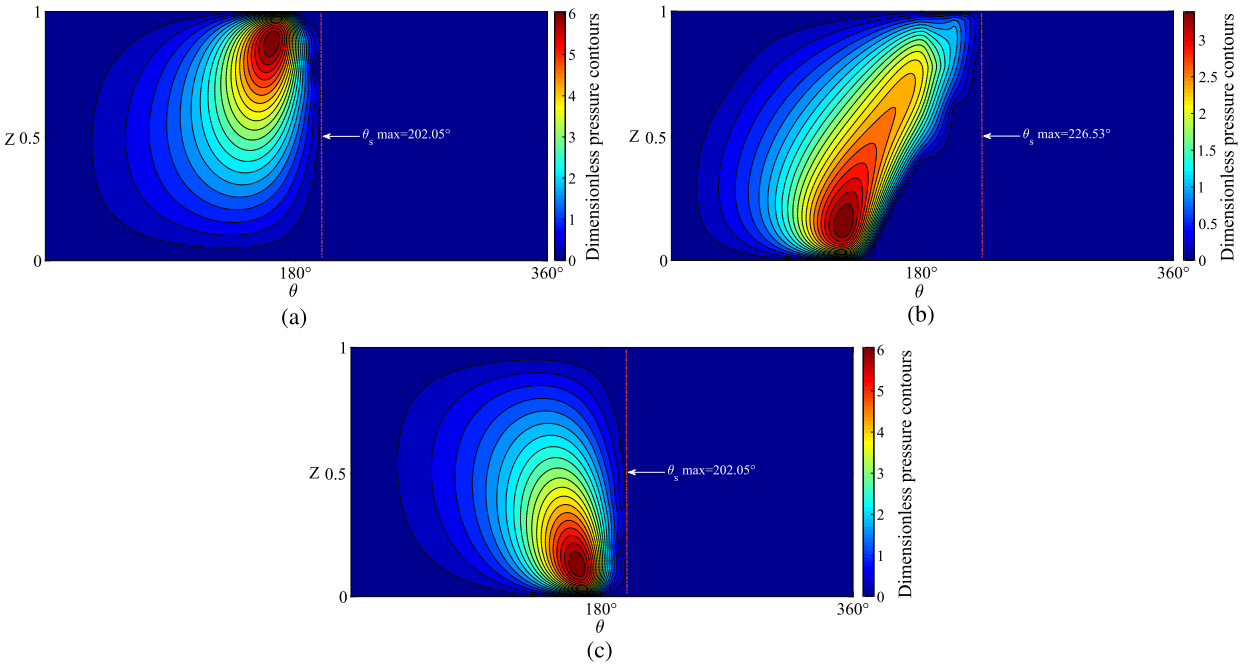

Fig. 19. Distribution of partially textured dimensionless pressure versus axial and circumferential coordinates for a misaligned journal bearing: (a) $\alpha = 0°$; (b) $\alpha = 90°$; (c) $\alpha = 180°$.

2.95, which corresponds to 3.71 MPa, while the maximum rupture angle reaches $\theta_{s\,max} = 189.80°$. Compared with the smooth bearing, in the fully textured case (Fig. 16b), the angular position of $\overline{P}_{max}$ moves backward near $\theta = 137.90°$, and its value decreases with about 56%, while the maximum rupture angle value increases by 6.12°. For partially textured case (Fig. 16c), the maximum pressure angular position moves forward near $\theta = 150.20°$, and, its value increases with about 5%, whereas, $\theta_{s\,max}$ increases by 12.25°. Note that, when the rupture angle value increases, the full film region increases and then the cavitation area is reduced, which causes the generation of additional hydrodynamic pressure and enhances the load lifting capacity. In the presence of misalignment ($D_m = 0.75$), the pressure distribution is plotted at various angles

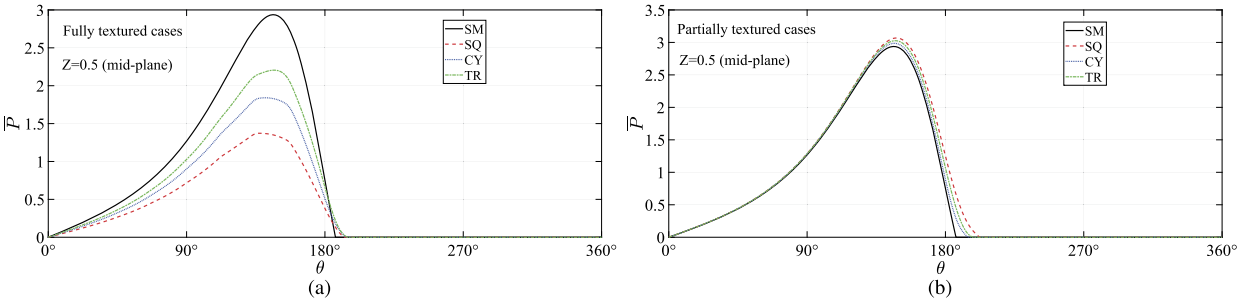

Fig. 20. Effect of texture shapes on the two-dimensional pressure distribution along the circumferential direction at the bearing's mid-plane for an aligned journal bearing: (a) fully textured cases (from 0° to 360°); (b) partially textured cases (from 180° to 360°).

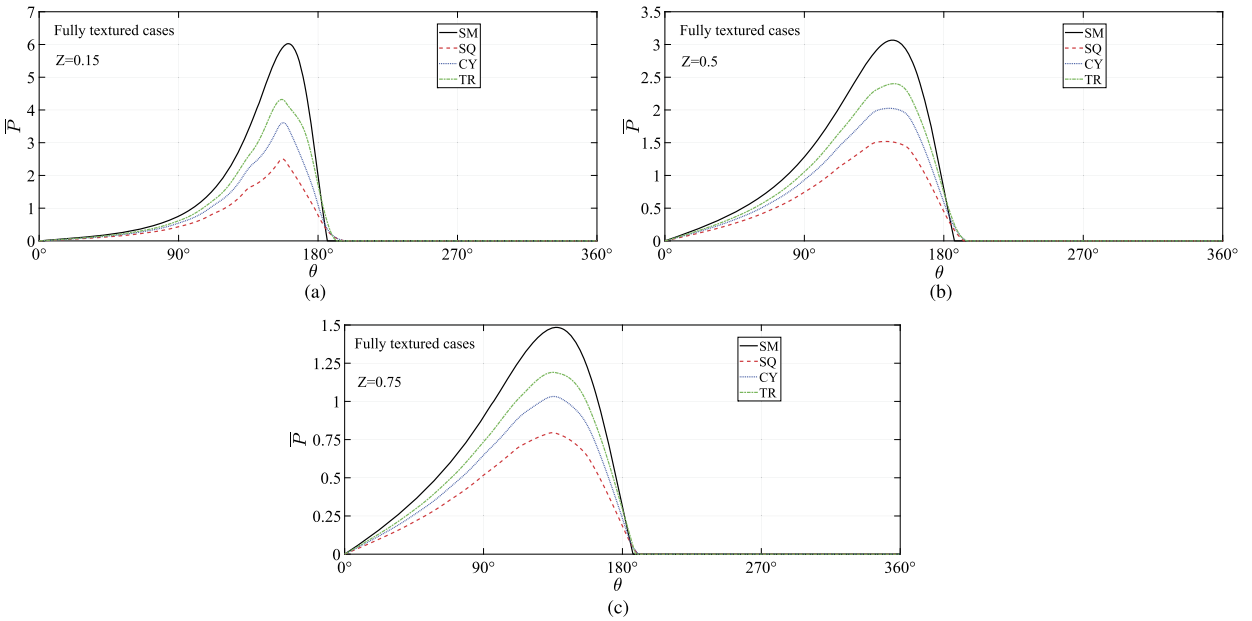

Fig. 21. Effect of fully texture shapes on the two-dimensional pressure distribution along the circumferential direction at: (a) $Z = 0.15$; (b) $Z = 0.5$; (c) $Z = 0.75$ for misaligned journal bearing ($D_m = 0.75$, $\alpha = 180°$).

of misalignment (Fig. 17, 18 and 19). From these figures, one very clearly sees that misalignment influenced the pressure fields in the axial direction and the location of the pressure peak. Compared to an aligned journal bearing, for smooth bearing (Fig. 17), the maximum pressure location is shifted to the rear end for $\alpha = 0°$ (Fig. 17a) and to the front end for $\alpha = 180°$ (Fig. 17c), whereas a single peak appears at the same circumferential location $\theta = 147.66°$, with the same value of about 6.13, which corresponds to 7.70 MPa, that is, twice larger than the aligned bearing, while the maximum rupture angle location remains constant at $\theta_{s\,max} = 189.80°$ for both cases. For $\alpha = 90°$ (Fig. 17b) the maximum pressure occurs for two values, near $\theta = 120°$ on the rear end and near $\theta = 190°$ on the front end, as a result of the two minimums of film thickness caused by this misalignment condition (Fig. 13c). The maximum rapture angle, also, is shifted to the rear end near $\theta_{s\,max} = 227.75°$. Compared with the misaligned smooth bearing, in the fully textured cases (Fig. 18), for $\alpha = 0°$ and $\alpha = 180°$, the location of $\overline{P}_{max}$ moves backward near $\theta = 144°$, and its value decreases by about 59%, while the maximum rupture angle value increases by 9.8°. For $\alpha = 90°$, the maximum pressure location moves backward and the maximum rupture angle value increases by about 2%. For the partially textured bearing cases (Fig. 19), the location of the pressure peak moves forward near $\theta = 150.10°$, for $\alpha = 0°$ and $\alpha = 180°$, and its value increases by about 4.8%, while $\theta_{s\,max}$ increases by 12.14°. Furthermore, for $\alpha = 90°$, the maximum pressure location moves forward, while the maximum rupture angle value decreases by 0.5%.

The effect of texture shapes on the two-dimensional 2D pressure profile for aligned/misaligned journal bearings is visualized in Figs. 20, 21, and 22. Each figure is plotted in circumferential direction, at the mid-plane for aligned bearings and in rear end ($Z = 0.15$), front end ($Z = 0.75$), and mid-plane ($Z = 0.5$) for misaligned bearings. In the absence of misalignment, in fully textured cases (Fig. 20a), the values of the dimensionless film pressure for all considered texture shapes are less than in the smooth case. This can be explained by the fact that dimple shapes with flat bottoms ("SQ", "CY" and "TR") have a micro-step bearing mechanism. Due to this mechanism, the micro-step bearing causes a much large film thickness

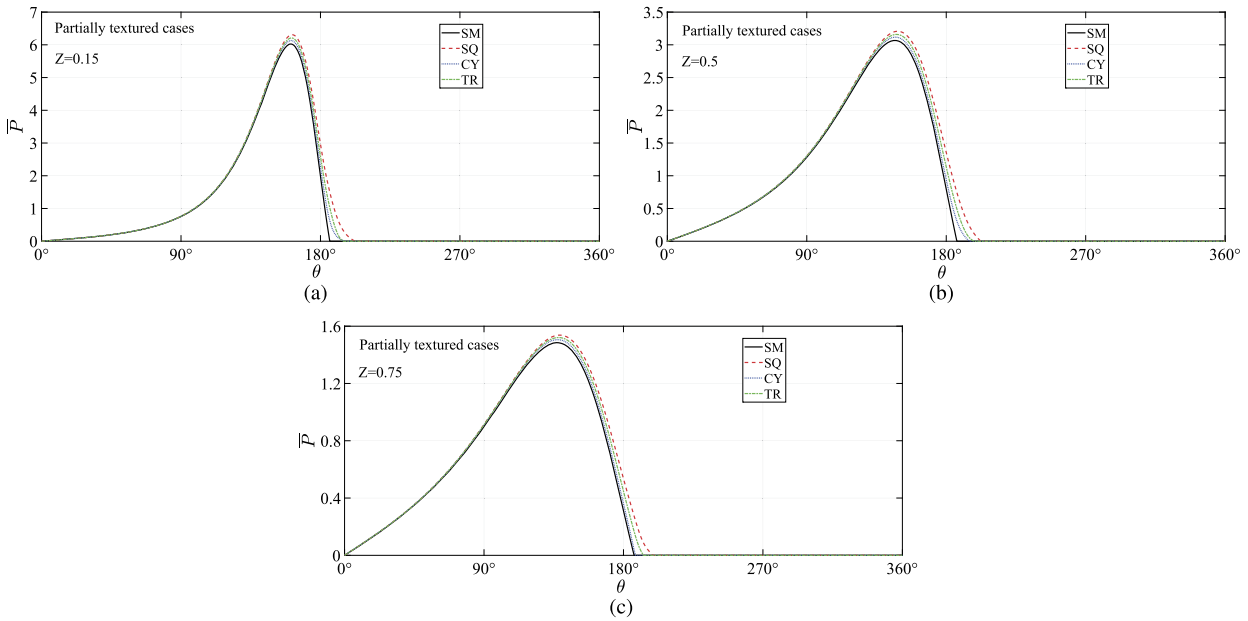

Fig. 22. Effect of partially texture shapes on the two-dimensional pressure distribution along the circumferential direction at: (a) $Z = 0.15$; (b) $Z = 0.5$; (c) $Z = 0.75$ for misaligned journal bearing ($D_m = 0.75$, $\alpha = 180°$).

divergence, so a significant pressure drop (in full-film region) and a smaller pressure recovery will be generated (in film rupture region). As the texture contour geometry increases, the micro-pressure drop effect increases. Unlike in the previous case, a significant improvement in the pressure profile caused by partially textured features is clearly shown in Fig. 20b, as a result of a micro-pressure recovery mechanism, which causes a nil pressure drop in full-film region and a higher pressure recovery will be generated in the film rupture region. For misaligned bearings, fully textured features (Fig. 21) reduce the pressure profile at any section, while partially textured features increase the pressure profile (Fig. 22) as a result of the micro-step bearing mechanism.

In the next subsections, the obtained results for smooth/textured misaligned bearing cases are compared in terms of: maximum pressure, leakage flow rate, load-carrying capacity, load-attitude angle, friction force and coefficient, misalignment moment and moment direction.

3.2.2. Influence of the degree of misalignment D_m

The curves of a number of bearing performance parameters as a function of the degree of misalignment are shown in Figs. 23a–23h (for smooth and full/partial textured bearing surface cases). Note that, in this subsection, the misalignment angle α is fixed at $\alpha = 180°$, while the degree of misalignment varies between 0 and 0.9.

The curves giving the dimensionless maximum pressure $\overline{P}_{max}$ for various degrees of misalignment D_m is shown in Fig. 23a. It is found that the rate of increase in $\overline{P}_{max}$ for all the considered cases is pronounced at higher values of the misalignment degree D_m (especially when $D_m > 0.5$), simply because of the smaller minimum film thickness. It should be emphasized that, when $D_m = 0$, the bearing is aligned, and, when $D_m \to 1$, the minimum film thickness $\overline{h}_{min} \to 0$ (the surfaces come into direct contact), and the maximum pressure $\overline{P}_{max} \to \infty$. Moreover, the previous figure also shows the comparative graph for smooth, fully, and partially textured bearing surfaces. The maximum pressure values are clearly different from those recorded for the smooth surface. In addition, it can be seen from this figure that the main feature of fully texturing bearing surfaces is to reduce the maximum pressure as a result of the micro-pressure drop effect, while partially texturing gradually increases the maximum pressure. This behavior is due to the dimple pressure recovery generated by the textures in the film rupture region.

In Fig. 23b, the leakage flow rate $\overline{Q}_Z$ slightly increases with increasing the degree of misalignment, which can be justified by the large pressure gradient on both ends. It is also visible that, in the case of fully textured bearings, all considered texture shapes reduce the leakage flow rate, which in fact results from the larger pressure drop by the presence of dimples in the full film bearing surface, while, in the case of partially textured bearings, all the considered dimples increase slightly the leakage flow rate, which is due to the fact that the pressure field tends to accumulate inside the texture cavity (micro-pressure recovery mechanisms) and thus adds a supplementary pressure that increases the pressure gradient.

Fig. 23c shows that the load-carrying capacity increases with increasing the degree of misalignment. Firstly, the increase in $\overline{W}_C$ follows the same trend as the previous dimensionless maximum pressure (Fig. 23a) for the smooth and full/partial textured cases. Secondly, texturing the whole bearing surface does not enhance the load carrying capacity, while partial

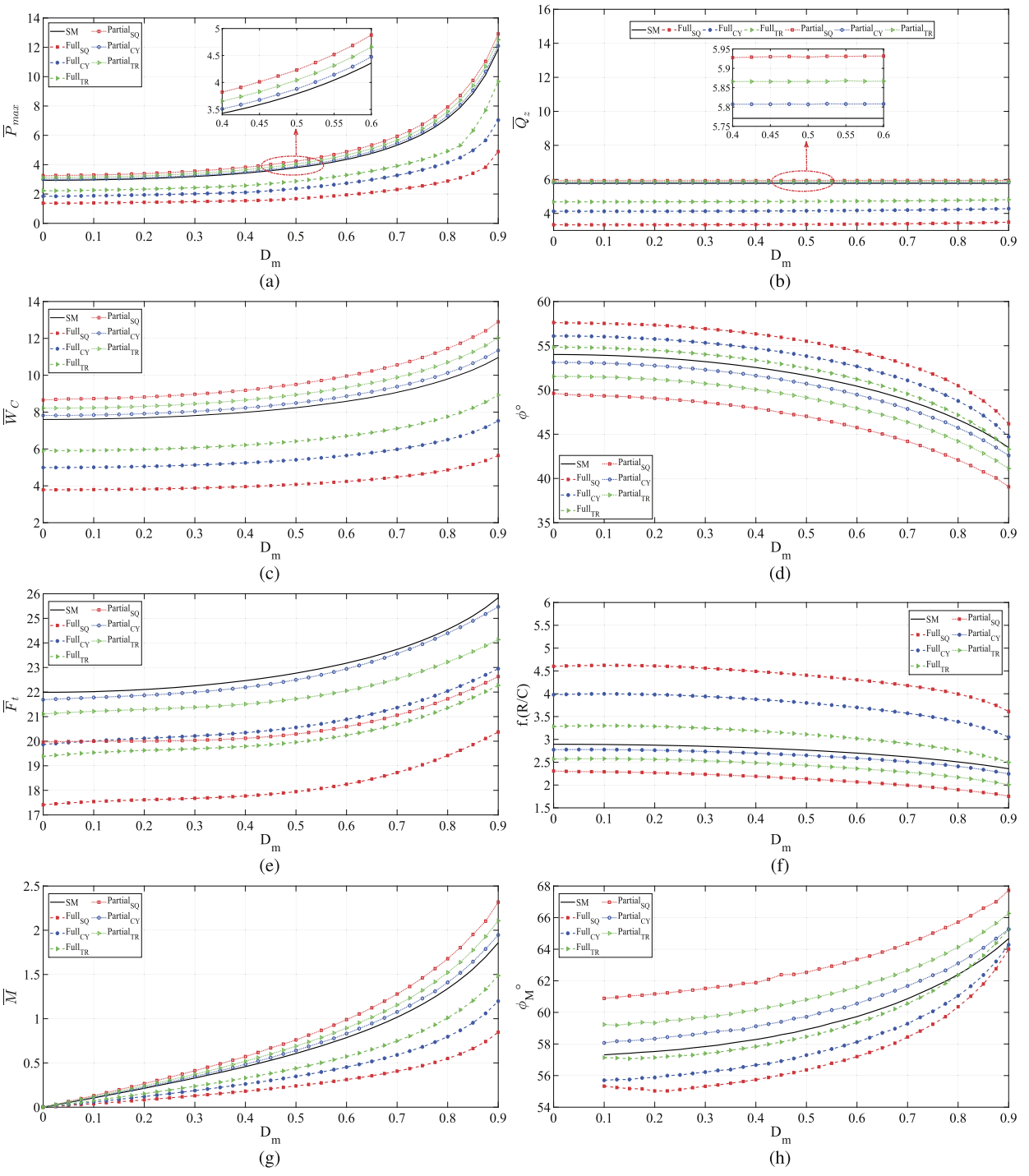

Fig. 23. Variation in bearing performances with the degree of misalignment for smooth/textured surface bearings for: $\Lambda = 1$; $\varepsilon = 0.6$; $\alpha = 180°$.

texturing causes a significant improvement of $\overline{W}_C$. These results can be justified by the presence of flat bottom profiles in the micro-step bearing mechanism (explained previously), which cause, in the full film region, a thicker film thickness, and so a largest pressure drop (presenting a bad performance in $\overline{W}_C$), while, in the film rupture region, a significant pressure recovery will be generated (with an improvement of $\overline{W}_C$). These results are consistent with those described in [64]. Here, an emphasis is placed on the texture contour geometry, which presents a key parameter in flat bottom profile contour geometry. In the fully texturing case, as the texture contour geometries increase, the micro-step bearing mechanism effects increase (highest film thickness divergence and largest pressure drop). In the partially texturing case, the square texture

shape performed the best hydrodynamic enhancement, followed by the triangle and the circle, which confirms the results obtained by Zhang et al. [69].

Beside the load-carrying capacity, Fig. 23d presents the variation of the load-attitude angle ϕ against the degree of misalignment D_{m} for smooth/textured surface bearings. It can be discerned from the figure that, for any studied texture shapes for the full/partial textured cases, the values of the load-attitude angle are obviously different from those of smooth surfaces. However, ϕ decreases with the increase in D_{m}; this decrease is more considerable at higher values of the degree of misalignment to support the large bearing load. For fully texturing features, the load attitude angle increases compared to the smooth surface bearing case, as a result of the decreasing load, while the main effect of partially texturing is to increase the load attitude angle compared to the smooth surface case, which is due to the increase of the bearing load.

The evolution of the dimensionless friction force F_t and of the friction coefficient $f\cdot(R/C)$ for different values of degree of misalignment D_{M} in the cases of smooth/textured surface bearings are shown in Figs. 23e and 23f, respectively. In Fig. 23e, it is noticed that, for all the considered configurations (smooth and full/partial textured surface bearing), the friction force increases with the increase of D_{m}, and one can also see that all texture features reduce the friction force. However, compared to the friction force (Fig. 23e), the resulting friction coefficients values follow an opposite trend. Moreover, it can be also observed that the friction coefficient $f\cdot(R/C)$ decreases with increasing the degree of misalignment D_{M} for all studied cases. However, in the case of fully textured bearings, the friction coefficients increase compared to the smooth surface case, presenting a bad performance. This is due to the fact that the flat bottom profiles cause a pressure drop, which decreases the load-carrying capacity, and so increases the friction values. In the other case of partially textured bearings, the square shape "SQ" shows the greatest friction reduction, followed by the triangle and the circle. This is due to the increase in the load-carrying capacity caused by the pressure recovery of these textures.

The total misalignment moment M and its direction angle ϕ_{M} are computed at the given misalignment conditions and plotted in Figs. 23g and 23h, respectively. It can be noticed that both the bearing moment and its direction angle increase with increasing the degree of misalignment. This is due to the larger pressure and its asymmetric shape. Furthermore, texturing the whole bearing surface reduces the bearing moment and the moment angle for any texture shapes, compared to the smooth surface, as a result of micro-pressure drop mechanisms. While, partially surface texturing increases the misalignment moment and its direction angle, presenting a good performance, which also results from texture micro-pressure recovery mechanisms.

3.2.3. Influence of the misalignment angle α

The bearing performance parameters at various angles of misalignment are presented in Table 5. Note that, in this subsection, the degree of misalignment D_{m} is fixed at $D_{\mathrm{m}} = 0.75$, while the angle of misalignment varies in the range from (0° to 180°). Moreover, the case where the misalignment angle varies from $180^\circ \rightarrow 360^\circ$ is not presented in the table, since both cases are physically the same, observed in an opposite direction (i.e. at $\alpha = 0^\circ$, the results are the same as those at $\alpha = 180^\circ$).

From the Table 5, it can be seen that the computed dimensionless maximum pressure and dimensionless leakage flow rate of smooth/textured journal bearings decrease till the position $\alpha = 90^\circ$ and then increase with increasing α. This behavior can be explained by the fact that the minimum film thickness increases with increasing α until $\alpha = 90^\circ$ and then decreases with increasing α. The other noticeable points in Table 5 are the decrease in the maximum pressure and leakage flow rate after the incorporating of textures in full bearing surface, which had been explained previously by the micro-pressure drop effect. Moreover, the increase in the maximum pressure and leakage flow rate when the second half of bearing surface is textured is a result of the micro-pressure recovery mechanism.

The variation of the dimensionless bearing load is similar to that of the dimensionless maximum pressure. As mentioned above, the produced pressure in partially textured surface bearing enhances the load lifting capacity, and so decreases the load attitude angle values and friction coefficient, while the fully textured cases cause a net load loss, and so increases the load attitude angle values and the friction coefficient. Table 5 also presents the variation of the dimensionless friction force; it can be noticed that, corresponding to each misalignment angle α, all textures reduce the computed friction force values. Moreover, it is worth noting that, when α approaches 0° or 180°, the misalignment moment and its direction increase. This can be explained by the fact that the maximum pressure occurs near the front or rear end. For any misalignment angle α, as the whole bearing surface is textured, the moment and its direction decrease, while the partially textured bearing surfaces improve the misalignment moment and its direction.

3.2.4. Influence of the eccentricity ratio ε

In the previous subsections, the effect of journal misalignment in smooth/textured bearing surfaces is studied by varying the misalignment angle (α from 0° to 180°), and degree (D_{m} from 0 to 0.9), while the eccentricity ratio ε was set to $\varepsilon = 0.6$. Here, various eccentricity ratios (ε from 0.5 to 0.9), fixed misalignment angle ($\alpha = 180^\circ$) and degree ($D_{\mathrm{m}} = 0.75$) are considered. Computed performance characteristics as a function of eccentricity ratios are plotted in Fig. 24a–24h. The results observed is that, as the eccentricity ratio increases, the dimensionless bearing performances, such as, maximum pressure, leakage flow rate, bearing load, friction force, and moment increase due to the decrease in the minimum film thickness, while the load attitude angle and friction coefficient decrease due to the large bearing load. Fully textured bearings have a detrimental effects (reducing the load-carrying capacity, the misalignment moment, and increasing the friction coefficient), while partially textured bearings perform better by increasing the load lifting capacity and the misalignment moment, and

Table 5
Variation in dimensionless bearing performances with the angle of misalignment for smooth/textured bearing surfaces for $\Lambda = 1$, $\varepsilon = 0.6$, and $D_m = 0.75$.

α			0°	30°	60°	90°	120°	150°	180°		0°	30°	60°	90°	120°	150°	180°
	SM		6.072	5.584	4.414	3.514	5.212	5.998	6.075		5.771	5.580	5.296	4.913	5.155	5.554	5.771
	SQ		2.638	2.362	1.887	1.551	2.220	2.426	2.554		3.479	3.336	3.157	2.988	3.073	3.287	3.412
Full textured	CY	Maximum pressure	3.701	3.312	2.684	2.151	3.138	3.536	3.647	Leakage flow rate	4.257	4.090	3.869	3.678	3.801	4.057	4.213
	TR		4.388	4.046	3.266	2.616	3.680	4.370	4.345		4.786	4.605	4.366	4.098	4.287	4.576	4.757
	SQ		6.710	6.108	4.638	3.516	5.223	6.040	6.751		5.927	5.620	5.305	4.989	5.183	5.603	5.934
Partial textured	CY		6.236	5.734	4.564	3.515	5.218	6.017	6.229		5.808	5.604	5.300	4.956	5.173	5.563	5.809
	TR		6.460	5.982	4.636	3.515	5.220	6.025	6.463		5.870	5.610	5.304	4.962	5.174	5.578	5.870
	SM		9.391	9.060	8.354	8.102	8.840	9.345	9.396		47.854	46.108	45.684	52.223	53.028	50.220	47.829
	SQ		4.774	4.605	4.141	4.077	4.440	4.615	4.645		51.064	48.863	49.812	53.308	55.996	54.118	51.802
Full textured	CY	Load-carrying capacity	6.310	6.116	5.521	5.424	5.941	6.185	6.211	Load-attitude angle	49.635	47.223	47.911	52.949	54.516	52.419	50.042
	TR		7.459	7.104	6.460	6.354	6.935	7.244	7.395		48.302	46.956	46.996	52.322	54.0176	51.669	48.488
	SQ		10.857	9.968	8.396	8.195	8.909	9.656	10.965		43.529	42.939	44.985	50.956	52.828	49.212	43.201
Partial textured	CY		9.723	9.395	8.363	8.161	8.853	9.493	9.718		46.863	45.065	45.489	51.482	53.009	49.743	46.867
	TR		10.230	9.631	8.374	8.163	8.894	9.506	10.249		45.441	44.024	45.078	51.034	52.869	49.744	45.377
	SM		24.104	47.574	45.346	39.266	29.986	27.950	24.104		2.5667	5.251	5.428	4.846	3.392	2.991	2.565
	SQ		19.064	29.943	28.458	24.859	19.998	18.473	18.954		3.993	6.503	6.871	6.097	4.504	4.003	4.081
Full textured	CY	Friction force	20.943	34.945	33.334	29.236	22.924	21.329	21.468	Friction coefficient	3.319	5.714	6.038	5.390	3.859	3.448	3.456
	TR		20.998	39.470	37.141	32.574	25.214	23.576	20.932		2.815	5.556	5.749	5.126	3.636	3.255	2.830
	SQ		21.502	31.911	31.539	29.007	24.592	23.288	21.380		1.980	3.201	3.766	3.540	2.760	2.412	1.950
Partial textured	CY		23.893	40.246	38.458	34.453	27.318	25.449	23.911		2.457	3.822	4.2682	3.945	2.942	2.602	2.460
	TR		22.936	36.808	35.696	32.204	26.167	24.703	22.824		2.242	4.284	4.580	4.221	3.086	2.677	2.227
	SM		1.162	1.114	0.953	0.864	0.946	1.114	1.163		61.552	73.583	87.901	30.887	28.530	48.851	61.575
	SQ		0.517	0.525	0.428	0.390	0.389	0.443	0.469		59.953	73.130	89.531	36.868	23.886	44.682	59.249
Full textured	CY	Misalignment moment	0.720	0.729	0.592	0.539	0.567	0.651	0.681	Misalignment direction	60.460	73.498	89.875	33.939	26.577	46.444	60.066
	TR		0.888	0.850	0.715	0.644	0.695	0.790	0.864		61.458	73.076	89.131	32.684	27.504	46.882	61.361
	SQ		1.437	1.380	1.033	0.958	0.957	1.120	1.462		64.717	75.841	88.738	32.009	29.387	49.826	65.016
Partial textured	CY		1.232	1.316	1.007	0.918	0.953	1.118	1.230		62.364	74.083	88.324	31.382	29.103	49.670	62.354
	TR		1.317	1.180	1.018	0.928	0.957	1.115	1.320		63.276	75.329	88.617	31.779	29.329	49.743	63.332

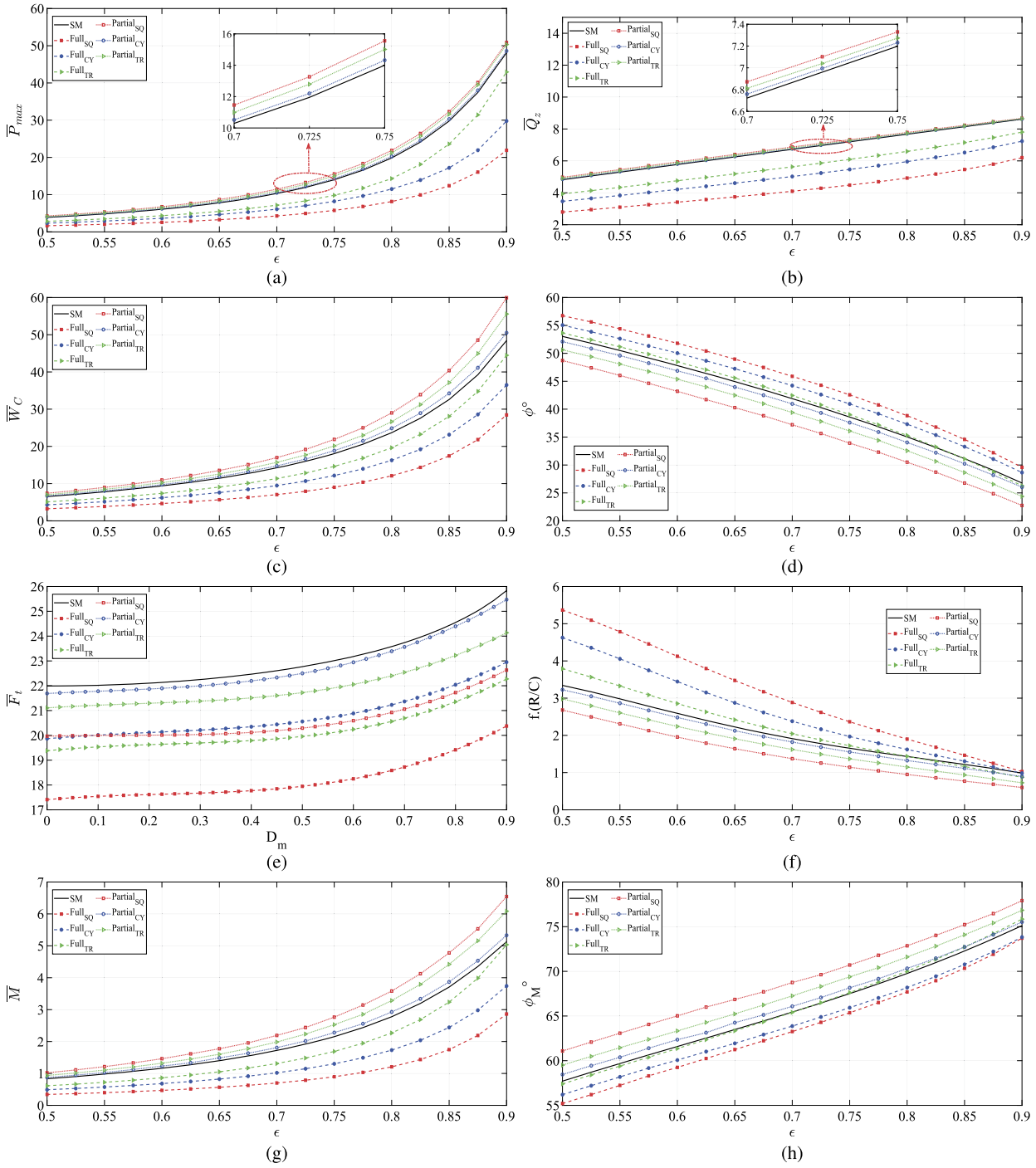

Fig. 24. Bearing performances versus eccentricity ratio for smooth/textured surface bearings for $\Lambda = 1$, $D_m = 0.75$, and $\alpha = 180°$.

by lowering the friction coefficient – this is more pronounced at higher values of eccentricity ratios ε. This is clearly due to the micro-step bearing effect, which can positively or negatively affect the tribological characteristics of the misaligned journal bearing (which depend mainly on the location of the texture zone).

4. Conclusion

In this paper, a numerical study was conducted to highlight the potential of the combined influences of bearing surface texturing and journal misalignment on the performance characteristics of hydrodynamic journal bearings. Three texture

shapes with flat bottoms: square (SQ), cylindrical (CY), and triangular (TR), as well as shaft misalignment variations in angle α, and degree D_{m} were considered. The model employed herein was solved by means of a finite difference technique by taking into account the rupture and reformation of the lubrication film by adopting the mass-conserving cavitation algorithm ("JFO" boundary conditions). The predictions made with the present numerical model were validated against available theoretical and experimental data in the literature.

The findings from the present numerical investigation can be summarized by the following points.

1. The texture contour geometry and its location has proved to be key parameters in journal bearing performances.
2. Fully textured bearing with flat/constant bottom dimples poorly affect the main bearing performances as compared to the smooth case, which is directed by the micro-pressure drop effect. Moreover, as the texture contour geometry increases, the micro-pressure drop effect increases, while partially texturing significantly enhance all bearing performances, which can be explained by the effect of the micro-pressure recovery mechanism. These facts were more noticeable at high eccentricity ratios, high misalignment degrees and when α approaches 0° or 180°.
3. The square "SQ" texture shape appears to be the most favorable one to improve the misaligned bearing performances, followed by the triangular "TR", then the cylindrical "CY".
4. As the degree of misalignment increases, the maximum pressure, the leakage flow rate, the bearing load, the friction force, and the moment increase due to a decrease in the minimum film thickness, while the load attitude angle and friction coefficient decrease due to the large bearing load. Also, the inclusion of textures at the requisite location can compensate the reduces bearing performances caused by shaft misalignment, especially when $\alpha \to 0°$ or $\alpha \to 180°$.
5. The previous observations about texturing the second angular part of the bearing (beyond 180°) are due to the micro-pressure recovery effect, which generates additional hydrodynamic pressure and serve as fluid reservoirs that provide lubricant to the contact in starvation cases, and so, enhance the main bearing performances.
6. The optimum textured location depends strongly on the geometrical parameters (type of misalignment) and the operating conditions of the journal bearings.

The conducted study is constrained by the selected texturing parameters; fixed density, number, disposition, orientation, and dimension; the chosen problem assumptions, by applying Newtonian rheology and mass-conserving cavitation; by the selected geometrical parameters: bearing length and diameter, eccentricity ratio and misalignment condition, and neglecting changes in viscosity, density and temperature, etc. On the one hand, breaking these constraints will open to us new possibilities of finding the optimum texture shapes required to each bearing configuration, on the other hand, difficulties on the computational aspect will be faced (CPU-time and cost). The need for efficient and fast algorithms becomes more than necessary. In this context, considerable efforts have been made by our research team to efficiently reduce the computation time using model order reduction (MOR) [74]. The application of this technique to the simulation of textured misaligned journal bearing is planned as the next step of this research.

Appendix A

e_0	Eccentricity at the bearing's mid-plane (m)
e'	Magnitude of the projection of the misaligned journal axis on the mid-plane (m)
C	Radial clearance (m)
D	Bearing diameter (m)
D_{m}	Degree of misalignment
L	Bearing length (m)
R	Bearing radius (m)
F	External applied force (N)
g	Cavitation switching function
U	Shaft speed ($^{\mathrm{m}}/_{\mathrm{s}}$)
x, y, z	Global Coordinate system (m)
r_x, r_z, r_y	Texture dimensions (m)
h	Film thickness (m)
Δh	Variation of film thickness due to the presence of the texture (m)
p	Lubricant pressure (Pa)
p_{c}	Cavitation pressure (Pa)
$p_{\max}$	Maximum pressure (Pa)
W_{C}	Load-carrying capacity
Q_z	Leakage flow rate (m^3/s)
F_t	Friction force (N·m)
$f.(^{R}/_{C})$	Friction coefficient
M	Misalignment moment (N·m)
nC_θ, nC_z	Number of textures along the circumferential θ and axial Z directions
tol_Θ	Relative convergence criterion on pressure

tol_{W}	Relative convergence criterion on load
tol_{M}	Relative convergence criterion on moment magnitude
$tol_{\phi_{\mathrm{M}}}$	Relative convergence criterion on moment direction
$\overline{P}_{\max}$	Dimensionless maximum pressure
$\overline{W}_{\mathrm{C}}$	Dimensionless load-carrying capacity
$\overline{Q_z}$	Dimensionless axial film flow
$\overline{F_t}$	Dimensionless friction force
$\overline{M}$	Dimensionless moment
$\overline{h}$	Dimensionless film thickness $[h/C]$
$\overline{h_s}$	Dimensionless equivalent of oil film thickness in cavitation zone
$\overline{\Delta h}$	Dimensionless variation of film thickness due to the presence of the texture
$\overline{P}$	Dimensionless lubricant pressure
$\overline{P_{\mathrm{c}}}$	Dimensionless cavitation pressure
$\theta, \overline{y}, Z$	Dimensionless global coordinate system
$\overline{r_x}, \overline{r_z}, \overline{r_y}$	Dimensionless texture dimensions
α	Angle between ϕ_0 and the rear center of the misaligned journal
β	Bulk modulus (Pa)
$\overline{\beta}$	Dimensionless bulk modulus
ρ	Fluid density of the oil (kg/m^3)
ρ_{c}	Fluid density at the cavitation pressure (kg/m^3)
Θ	Fractional film content $\Theta = \rho/\rho_{\mathrm{c}}$
Λ	Aspect ratio $\Lambda = L/D$
ϕ	Attitude angle (°)
ϕ_{M}	Misalignment direction (°)
ω	Angular velocity (rad/s)
μ	Dynamic viscosity (Pa·s)
ε	Eccentricity ratio $\varepsilon = e_0/C$
ε'	Misalignment eccentricity ratio $\varepsilon' = e'/C$
θ_s	Angular position of the rupture zone (°)

References

[1] M.M. Khonsari, E.R. Booser, Applied Tribology: Bearing Design and Lubrication, vol. 12, John Wiley & Sons, 2008.
[2] R.A. Mufti, M. Priest, Theoretical and experimental evaluation of engine bearing performance, Proc. Inst. Mech. Eng., Part J J. Eng. Tribol. 223 (4) (2009) 629–644.
[3] J.Y. Jang, M.M. Khonsari, On the characteristics of misaligned journal bearings, Lubricants 3 (1) (2015) 27–53.
[4] S.A. McKee, T.R. McKee, Pressure distribution in oil films of journal bearings, Tribol. Int. 57 (1932) 149–165.
[5] G.B. Dubois, H.H. Mabie, F.W. Ocvirk, Experimental Investigation of Oil Film Pressure Distribution for Misaligned Plain Bearings, NACA Technical Note 2507(3), 1951.
[6] G.B. DuBois, F.W. Ocvirk, R.L. Wehe, Properties of misaligned journal bearings, Trans. Amer. Soc. Mech. Eng. 79 (1205-1) (1957) 2.
[7] A.J. Smalley, H. McCallion, Paper 5: the effect of journal misalignment on the performance of a journal bearing under steady running conditions, in: Proceedings of the Institution of Mechanical Engineers, Conference Proceedings, vol. 181, SAGE Publications Sage UK, London, England, 1966, pp. 45–54.
[8] D.V. Singh, R. Sinhasan, R. Pal, Performance characteristics of an ungrooved big-end bearing with misalignment, Tribol. Trans. 32 (2) (1989) 234–238.
[9] J.R. Stokley, R.R. Donaldson, Misalignment effects in 180° partial journal bearings, ASLE Trans. 12 (3) (1969) 216–226.
[10] J.S. Ausman, Torque produced by misalignment of hydrodynamic gas-lubricated journal bearings, J. Basic Eng. 82 (2) (1960) 335–340.
[11] J.R. Rice, Misalignment torques of hydrodynamic gas-lubricated journal bearings, J. Basic Eng. 87 (1) (1965) 193–198.
[12] P. Monmousseau, M. Fillon, Analysis of static and dynamic misaligned tilting-pad journal bearings, Proc. Inst. Mech. Eng., Part J J. Eng. Tribol. 213 (4) (1999) 253–261.
[13] A.M. El-Butch, N.M. Ashour, Transient analysis of misaligned elastic tilting-pad journal bearing, Tribol. Int. 38 (1) (2005) 41–48.
[14] L. San Andres, The effect of journal misalignment on the operation of a turbulent flow hydrostatic bearing, J. Tribol. 115 (3) (1993) 355–363.
[15] S.C. Jain, S.C. Sharma, T. Nagaraju, Misaligned journal effects in liquid hydrostatic non-recessed journal bearings, Wear 210 (1–2) (1997) 67–75.
[16] J.O. Medwell, D.T. Gethin, Synthesis of thermal effects in misaligned hydrodynamic journal bearings, Int. J. Numer. Methods Fluids 6 (7) (1986) 445–458.
[17] P. Arumugam, S. Swarnamani, B.S. Prabhu, Effects of journal misalignment on the performance characteristics of three-lobe bearings, Wear 206 (1–2) (1997) 122–129.
[18] O. Pinkus, S.S. Bupara, Analysis of misaligned grooved journal bearings, J. Lubr. Technol. 101 (4) (1979) 503–509.
[19] K. Ikeuchi, S. Katsuse, K. Hamamura, H. Mori, Effects of misalignment in full journal bearing with circumferential oil groove, in: Proceedings of the JSLE International Tribology Conference, Tokyo, Japan, vol. 101, 1985, pp. 67–72.
[20] D. Vijayaraghavan, T.G. Keith, Effect of cavitation on the performance of a grooved misaligned journal bearing, Wear 134 (1989) 377–397.
[21] D. Vijayaraghavan, T.G. Keith, Analysis of a finite grooved misaligned journal bearing considering cavitation and starvation effects, ASME J. Tribol. 112 (1990) 60–67.
[22] J. Bouyer, M. Fillon, Improvement of the THD performance of a misaligned plain journal bearing, J. Tribol. 125 (2) (2003) 334–342.
[23] J.Y. Jang, M.M. Khonsari, On the behavior of misaligned journal bearings based on mass-conservative thermohydrodynamic analysis, J. Tribol. 132 (1) (2010) 011702.
[24] P. Kumar, M.M. Khonsari, Traction in EHL line contacts using free-volume pressure–viscosity relationship with thermal and shear-thinning effects, J. Tribol. 131 (1) (2009) 011503.
[25] Z.-p. He, J.-h. Zhang, W.-s. Xie, Z.-y. Li, G.-c. Zhang, Misalignment analysis of journal bearing influenced by asymmetric deflection, based on a simple stepped shaft model, J. Zhejiang Univ. Sci. A 13 (9) (2012) 647–664.

[26] A.A. Elsharkawy, Effects of misalignment on the performance of flexible porous journal bearings, Tribol. Trans. 46 (1) (2003) 119–127.
[27] S.D. Gulwadi, G. Shrimpling, Journal Bearing Analysis in Engines Using Simulation Techniques, Tech. rep., SAE Technical Paper, 2003.
[28] Z.S. Safar, M.M. Elkotb, D.M. Mokhtar, Analysis of misaligned journal bearings operating in turbulent regime, J. Tribol. 111 (2) (1989) 215–219.
[29] G. Xu, J. Zhou, H. Geng, M. Lu, L. Yang, L. Yu, Research on the static and dynamic characteristics of misaligned journal bearing considering the turbulent and thermohydrodynamic effects, J. Tribol. 137 (2) (2015) 024504.
[30] T.A. Osman, Misalignment effect on the static characteristics of magnetized journal bearing lubricated with ferrofluid, Tribol. Lett. 11 (3–4) (2001) 195–203.
[31] S. Das, S.K. Guha, A.K. Chattopadhyay, On the steady-state performance of misaligned hydrodynamic journal bearings lubricated with micropolar fluids, Tribol. Int. 35 (4) (2002) 201–210.
[32] X. Zhang, Z. Yin, D. Jiang, G. Gao, Y. Wang, X. Wang, Load carrying capacity of misaligned hydrodynamic water-lubricated plain journal bearings with rigid bush materials, Tribol. Int. 99 (2016) 1–13.
[33] L.A. Abdel-Latif, M.O.A. Mokhtar, Misalignment effects on hydrodynamically lubricated journal bearings with rough surfaces, Wear 128 (3) (1988) 225–237.
[34] S.K. Guha, Analysis of steady-state characteristics of misaligned hydrodynamic journal bearings with isotropic roughness effect, Tribol. Int. 33 (1) (2000) 1–12.
[35] S.C. Sharma, S.C. Jain, T. Nagaraju, Combined influence of journal misalignment and surface roughness on the performance of an orifice compensated non-recessed hybrid journal bearing, Tribol. Trans. 45 (4) (2002) 457–463.
[36] J. Sun, M. Deng, Y. Fu, C. Gui, Thermohydrodynamic lubrication analysis of misaligned plain journal bearing with rough surface, J. Tribol. 132 (1) (2010) 011704.
[37] N. Patir, H.S. Cheng, An average flow model for determining effects of three-dimensional roughness on partial hydrodynamic lubrication, J. Lubr. Technol. 100 (1) (1978) 12–17.
[38] N. Patir, H.S. Cheng, Application of average flow model to lubrication between rough sliding surfaces, J. Lubr. Technol. 101 (2) (1979) 220–229.
[39] M. Qiu, B.R. Minson, B. Raeymaekers, The effect of texture shape on the friction coefficient and stiffness of gas-lubricated parallel slider bearings, Tribol. Int. 67 (2013) 278–288.
[40] I. Etsion, State of the art in laser surface texturing, Trans. ASME F J. Tribol. 127 (1) (2005) 248.
[41] X. Wang, K. Kato, Improving the anti-seizure ability of SiC seal in water with RIE texturing, Tribol. Lett. 14 (4) (2003) 275–280.
[42] L.S. Stephens, R. Siripuram, M. Hayden, B. McCartt, Deterministic micro asperities on bearings and seals using a modified LIGA process, in: ASME Turbo Expo 2002: Power for Land, Sea, and Air, American Society of Mechanical Engineers, 2002, pp. 573–580.
[43] Y.G. Schneider, Formation of surfaces with uniform micropatterns on precision machine and instruments parts, Precis. Eng. 6 (4) (1984) 219–225.
[44] A. Greco, S. Raphaelson, K. Ehmann, Q.J. Wang, C. Lin, Surface texturing of tribological interfaces using the vibromechanical texturing method, J. Manuf. Sci. Eng. 131 (6) (2009) 061005.
[45] M. Wakuda, Y. Yamauchi, S. Kanzaki, Y. Yasuda, Effect of surface texturing on friction reduction between ceramic and steel materials under lubricated sliding contact, Wear 254 (3) (2003) 356–363.
[46] D.B. Hamilton, J.A. Walowit, C.M. Allen, A theory of lubrication by micro-irregularities, J. Basic Eng. 88 (1) (1966) 177–185.
[47] D. Gropper, L. Wang, Terry J. Harvey, Hydrodynamic lubrication of textured surfaces: a review of modeling techniques and key findings, Tribol. Int. 90 (2016) 509–529.
[48] M. Varenberg, G. Halperin, I. Etsion, Different aspects of the role of wear debris in fretting wear, Wear 252 (11) (2002) 902–910.
[49] H. Yamakiri, S. Sasaki, T. Kurita, N. Kasashima, Effects of laser surface texturing on friction behavior of silicon nitride under lubrication with water, Tribol. Int. 44 (5) (2011) 579–584.
[50] X. Lu, M.M. Khonsari, An experimental investigation of dimple effect on the Stribeck curve of journal bearings, Tribol. Lett. 27 (2) (2007) 169.
[51] N. Tala-Ighil, M. Fillon, A numerical investigation of both thermal and texturing surface effects on the journal bearings static characteristics, Tribol. Int. 90 (2015) 228–239.
[52] N. Tala-Ighil, M. Fillon, P. Maspeyrot, Effect of textured area on the performances of a hydrodynamic journal bearing, Tribol. Int. 44 (3) (2011) 211–219.
[53] S. Kango, R.K. Sharma, R.K. Pandey, Thermal analysis of microtextured journal bearing using non-Newtonian rheology of lubricant and JFO boundary conditions, Tribol. Int. 69 (2014) 19–29.
[54] H.G. Elrod, M.L. Adams, A computer program for cavitation and starvation problems, in: Cavitation and Related Phenomena in Lubrication, vol. 103, 1974, pp. 37–41.
[55] H. Zhang, G. Dong, M. Hua, F. Guo, K.S. Chin, Parametric design of surface textures on journal bearing, Ind. Lubr. Tribol. 67 (4) (2015) 359–369.
[56] J.N. Anno, J.A. Walowit, C.M. Allen, Microasperity lubrication, J. Lubr. Technol. 90 (2) (1968) 351–355.
[57] K. Tønder, Inlet roughness tribodevices: dynamic coefficients and leakage, Tribol. Int. 34 (12) (2001) 847–852.
[58] K. Tønder, Hydrodynamic effects of tailored inlet roughnesses: extended theory, Tribol. Int. 37 (2) (2004) 137–142.
[59] I. Etsion, L. Burstein, A model for mechanical seals with regular microsurface structure, Tribol. Trans. 39 (3) (1996) 677–683.
[60] A.V. Olver, M.T. Fowell, H.A. Spikes, I.G. Pegg, 'Inlet suction', a load support mechanism in non-convergent, pocketed, hydrodynamic bearings, Proc. Inst. Mech. Eng., Part J J. Eng. Tribol. 220 (2) (2006) 105–108.
[61] M. Fowell, A.V. Olver, A.D. Gosman, H.A. Spikes, I. Pegg, Entrainment and inlet suction: two mechanisms of hydrodynamic lubrication in textured bearings, J. Tribol. 129 (2) (2007) 336–347.
[62] K. Yagi, J. Sugimura, Balancing wedge action: a contribution of textured surface to hydrodynamic pressure generation, Tribol. Lett. 50 (3) (2013) 349–364.
[63] T. Nanbu, N. Ren, Y. Yasuda, D. Zhu, Q.J. Wang, Micro-textures in concentrated conformal-contact lubrication: effects of texture bottom shape and surface relative motion, Tribol. Lett. 29 (3) (2008) 241–252.
[64] M.S. Uddin, T. Ibatan, S. Shankar, Influence of surface texture shape, geometry and orientation on hydrodynamic lubrication performance of plane-to-plane slider surfaces, Lubr. Sci. 29 (3) (2017) 153–181.
[65] B. Jakobsson, The Finite Journal Bearing Considering Vaporization, Trans. Chalmers Univ. of Tech, Sweden, vol. 190, 1965.
[66] K.-O. Olsson, Cavitation in Dynamically Loaded Bearing, Trans. Chalmers Univ. of Tech, Sweden, vol. 308, 1957.
[67] R. Ausas, P. Ragot, J. Leiva, M. Jai, G. Bayada, G.C. Buscaglia, The impact of the cavitation model in the analysis of microtextured lubricated journal bearings, J. Tribol. 129 (4) (2007) 868–875.
[68] P. Maspeyrot, J. Frene, Paper iii (i) comparison between aligned and misaligned bearings under dynamic loading in both quasi-static and dynamic misalignment, Tribol. Ser. 18 (7) (1991) 19–26.
[69] Y.L. Zhang, X.G. Zhang, G. Matsoukas, Numerical study of surface texturing for improving tribological properties of ultra-high molecular weight polyethylene, Biosurf. Biotribol. 1 (4) (2015) 270–277.
[70] A. de Kraker, R.A. van Ostayen, A. Van Beek, D.J. Rixen, A multiscale method modeling surface texture effects, J. Tribol. 129 (2) (2007) 221–230.
[71] D. Vijayaraghavan, T.G. Keith, An efficient, robust, and time accurate numerical scheme applied to a cavitation algorithm, J. Tribol. 112 (1) (1990) 44–51.
[72] M. Fesanghary, M.M. Khonsari, A modification of the switch function in the Elrod cavitation algorithm, J. Tribol. 133 (2) (2011) 024501.
[73] W.H. Press, The Art of Scientific Computing, Cambridge University Press, 1992.
[74] B. Cherabi, A. Hamrani, I. Belaidi, S. Khelladi, F. Bakir, An efficient reduced-order method with PGD for solving journal bearing hydrodynamic lubrication problems, C. R., Méc. 344 (10) (2016) 689–714.